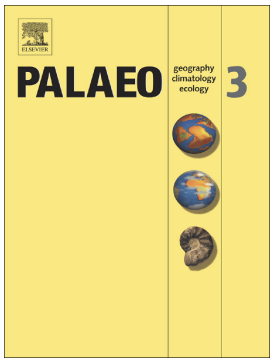

Mid-Albian to earliest Cenomanian climate cycles indicated by humid paleosols developed within the arid braidplain facies of the Utrillas Group of east-central Spain

Carlos A. Bueno-Cebollada, Raúl de la Horra, José F. Barrenechea, Nieves Meléndez, Eduardo Barrón, Marían Fregenal-Martínez

PII: S0031-0182(23)00319-X

DOI: https://doi.org/10.1016/j.palaeo.2023.111701

Reference: PALAEO 111701

To appear in: *Palaeogeography, Palaeoclimatology, Palaeoecology*

Received date: 20 April 2023

Revised date: 26 June 2023

Accepted date: 26 June 2023

Please cite this article as: C.A. Bueno-Cebollada, R. de la Horra, J.F. Barrenechea, et al., Mid-Albian to earliest Cenomanian climate cycles indicated by humid paleosols developed within the arid braidplain facies of the Utrillas Group of east-central Spain, *Palaeogeography, Palaeoclimatology, Palaeoecology* (2023), https://doi.org/10.1016/j.palaeo.2023.111701

Mid-Albian to earliest Cenomanian climate cycles indicated by humid paleosols developed within the arid braidplain facies of the Utrillas Group of east-central Spain.

Carlos A. Bueno-Cebollada[a] *, Raúl de la Horra[b], José F. Barrenechea [c], Nieves Meléndez[b], Eduardo Barrón[a], Marían Fregenal-Martínez[b].

[a] Instituto Geológico y Minero de España, Consejo Superior de Investigaciones Científicas (CN IGME-CSIC), c/ Ríos Rosas 23, 28003 Madrid (Spain).

[b] Departamento de Geodinámica, Estratigrafía y Paleontología, Facultad de Ciencias Geológicas, Universidad Complutense de Madrid, c/ José Antonio Nováis 12, 28040 Madrid (Spain)

[c] Departamento de Mineralogía y Petrología, Facultad de Ciencias Geológicas, Universidad Complutense de Madrid, c/ José Antonio Nováis 12, 28040 Madrid (Spain)

* Corresponding author

Keywords: Albian, Palaeoclimate, Eastern Iberia, Cuenca Basin, Utrillas Group

Abstract

The development of arid climate conditions in eastern Iberia during the mid-Cretaceous (mid-Albian to earliest Cenomanian) has been postulated by several authors over the last two decades based on sedimentological and palaeobotanical datasets. In this paper, we present a combined sedimentological and paleosol study of the mid-Albian to earliest Cenomanian Utrillas Group in the Cuenca Basin of east-central Spain, to improve knowledge of palaeoclimate. Four facies associations are identified as follows: Proximal alluvial braidplain (FA I), Distal alluvial braidplain (FA II), Aeolian dunes (FA III), and Inner estuarine settings (FA IV). The succession records the development of a braidplain system under dominantly arid conditions followed by a marine transgressive phase. In contrast to the overall arid palaeoclimate interpretation, multi-proxy palaeoedaphological analyses conducted for three paleosol profiles (Spodosols) indicate the occurrence of periods of increased humidity in the basin. These findings allow us to infer the

occurrence of shorter-term climatic oscillations characterised by a tropical savanna climate when the palaeosols developed, suggesting significantly more humid conditions than those inferred based on the sedimentological and previous palaeobotanical datasets. We propose a palaeoclimatic model that explains the alternation between the dominantly arid and these more humid periods based on the cyclical latitudinal shifting of the mid-Cretaceous climatic belts, shedding new light on the mid-Albian to earliest Cenomanian climate of Iberia.

1. Introduction

The mid-Cretaceous (110 – 90 ma) is a time span characterised by the highest global sea levels of the Phanerozoic (Haq, 2014), which gave rise to seaways that flooded large continental areas worldwide. This time interval is referred to as a global warming period dominated by greenhouse conditions, presenting shallow equator-pole temperature gradients and an absence of polar ice caps (Spicer and Corfield, 1992; Barron et al., 1995). This warm and latitudinally more constant climate has been related to the arrangement of the continental landmasses, mainly clustered in the low latitudes, and the high CO_2 levels that prevailed during the whole Cretaceous period (i.e., Arthur et al., 1985, 1990). Such high CO_2 levels were a function of the massive volcanism due to seafloor spreading during Pangaea's final break-up and the progressive formation of the Atlantic Ocean (Dallmann, 2015).

The data indicate that the global temperatures were relatively lower during the Aptian, notably increasing during the Albian, and leading to the Late Cretaceous thermal maximum during Cenomanian/Turonian ages (Norris et al., 2002; Puceat et al., 2003; Forster et al., 2007). Conversely, a cooling trend dominated the Late Cretaceous times, starting after the Cenomanian – Turonian boundary, which seems to conform with a decrease in atmospheric CO_2 (Spicer and Corfield, 1992). The common occurrence of conifer-dominated forests extending across the northern high latitudes (60° – 85°N) seems to indicate a cool temperate climate in those areas during late Albian to early Cenomanian times, which might have varied between ~1–10°C (mean annual temperature) (Spicer and Parrish, 1986; Spicer and Cornfield, 1992; Harland et al., 2007). In mid-latitudes, mega thermal floras extended up to 45° – 50°N due to the warm

temperatures that characterised the mid-Cretaceous (i.e., Spicer and Parrish et al., 1986; Fenner, 2001; Kvaček, 2003; Kvaček et al., 2005), giving rise to a mid-latitude warm humid climate belt (Corentin et al., 2020).

During mid-Albian to early Cenomanian times, Iberia was located at around 25° – 30°N latitude (i.e., Chumakov et al., 1995; Burgener et al., 2023) and mainly under the influence of a low latitude arid climate belt in its eastern part (Rodríguez-López et al., 2012), the Northern Hot Arid (NHA) belt. In this regard, previous sedimentological, palaeobotanical, and mineralogical data indicate that arid conditions prevailed in eastern Iberia (i.e., Rodríguez-López et al., 2008, 2009, 2010, 2012, 2013; Bueno-Cebollada et al., 2021, 2022; Barrón et al., 2023) from late mid-Albian to early Cenomanian times. The mid-Albian to lower Cenomanian deposits of the Iberian Basin Rift System (central east Spain; Martín-Chivelet et al., 2019a, b) are represented by the Utrillas Group (Gr), which has been interpreted as an erg system (aeolian desert) in the Maestrazgo Basin (i.e., Rodríguez-López et al., 2008, 2009, 2013) and as an arid braidplain system in the Cuenca Basin (Chamizo-Borreguero et al., 2016; Bueno-Cebollada and Meléndez, 2018; Bueno-Cebollada et al., 2021, 2022) (Fig. 1). The development of an ecosystem dominated by xerophytic taxa in the Cuenca Basin during mid-Albian to early Cenomanian (Barron et al., 2023) agrees with previous works dealing with the sedimentology of the Utrillas Gr both in the study area (Chamizo-Borreguero et al., 2016; Bueno-Cebollada et al., 2018) and to the east of the study area, in the Maestrazgo Basin (Rodríguez-López et al., 2008, 2009, 2010, 2012). Therefore, the Utrillas Gr succession was deposited in a predominantly arid setting.

Although the influence of the Northern Hot Arid (NHA) Belt dominated the climate of eastern Iberia, the proximity to the boundary with the Northern Mid-Latitude Humid (NMH) Belt (Chumakov et al., 1995; Hay and Floegel, 2012) has been proposed to explain the recorded climate oscillations between dry and more humid periods, due to the contraction and expansion of both climate belts during the mid-Albian to early Cenomanian (Rodríguez-López et al., 2012; Bueno-Cebollada et al., 2021). Rodríguez-López et al. (2012) suggest the occurrence of climate

forcing controlled by orbitally-induced latitudinal shifts as the main driver to explain the alternation of arid and more humid periods during the late Albian to early Cenomanian in the Maestrazgo Basin (IBRS, Eastern Spain). These latitudinal shifts, mainly controlled by the precession cycle (approx. 20 ka) and modulated by eccentricity at different scales (100 ka, 400 ka, 1.3 Ma, and 2 Ma), gave rise to the expansion and contraction of the boundaries of the NHA and NWM belts (Rodríguez-López et al., 2012).

The occurrence of sedimentary features that conform with the description of paleosols (i.e., root traces) in the Utrillas Gr succession is mentioned in the literature (i.e., Platt, 1989; Marfil et al., 1992; Chamizo-Borreguero et al., 2008, 2016; Bueno-Cebollada and Meléndez, 2018). However, to date, there is a lack of works dealing with the study of these paleosols and their palaeoclimatic implications. In this regard, the study of paleosols may shed light on sediment deposition and its relationship with the autogenic and allogenic factors of a sedimentary basin (Yaalon, 1971, 1983; Kraus, 1999). However, one of the most insightful applications of paleosols is that they can be considered reliable palaeoclimate indicators, useful when estimating mean annual palaeotemperatures and palaeoprecipitation rates (Mack, 1992; Kraus, 1999). Additionally, the combination of sedimentological and palaeoedaphological proxies provides an even more resourceful tool for understanding ancient alluvial systems and their allogenic controls, in particular climate (i.e., De la Horra et al., 2008; Varela et al., 2021).

In this paper, we present the study of three exceptionally well-preserved sequences of paleosols interbedded with the arid braidplain deposits of the mid-Albian to early Cenomanian Utrillas Gr succession in the Cuenca Basin (IBRS, central Spain), aiming to provide new reliable evidence on the palaeoclimatic conditions. The analysed sedimentary succession has been dated in the study area as mid-Albian to early Cenomanian age, based on pollen and spore associations, whose proportions and taxa reflect the dominance of drought-adapted vegetation mainly characterised by conifers of the families Cheirolepidaceae and Cupressaceae (Bueno-Cebollada et al., 2021; Bueno-Cebollada, 2022).

The aims and scope of this paper include:

i) the sedimentary facies analysis of the Utrillas Gr succession in the studied site and its paleoenvironmental meaning.

ii) the petrographical, mineralogical, and geochemical characterisation of the paleosols of the Utrillas Gr as palaeoclimate indicators.

iii) the interpretation of the palaeoclimate conditions that existed during the mid-Albian to early Cenomanian interval in the Cuenca Basin based on a combined approach which includes the mineralogical/geochemical analyses of the paleosols, sedimentological analysis of the Utrillas Gr deposits, and the integration of our results within the regional palaeoclimatic framework.

2. Geological Setting

The Iberian Basin Rift System (IBRS; formerly known as the Iberian Basin) comprises the intraplate Mesozoic rift basins of Iberia and occupies most of eastern and north-central Spain (Sopeña et al., 2004; Martin-Chivelet et al., 2019a). The IBRS is divided into five main palaeogeographical basins, namely: Cameros (northwestern), Maestrazgo (eastern), Central, Valencia (southeastern) and Cuenca (southwestern) Basins (Fig. 1A, B) (Aurell et al., 2019; Martín-Chivelet et al., 2019a). The study area of this paper is located in the Serranía de Cuenca, a geographical region that coincides with the southern part of the Cuenca Basin (Bueno-Cebollada et al., 2021).

The IBRS developed in relation to two phases of rifting, each preceded by post-rift phases when passive margin deposition and thermal subsidence dominated (Sopeña et al., 2004; Gómez et al., 2019). The first of these two rifting phases spanned the early Permian to latest Triassic (López-Gómez et al., 2019), while the second started during the Middle – Late Jurassic boundary and lasted until the late Albian (latest Early Cretaceous) (Sopeña et al. 2004; Aurell et al., 2019; Martín-Chivelet et al., 2019). The onset of a passive margin stage during the Late Cretaceous has been related to the deposition of the Utrillas Gr, which is traditionally considered the first post-rift sedimentary unit in the IBRS (Sopeña et al., 2004; Martín-Chivelet et al., 2019a, b).

The Utrillas Gr, originally defined with the rank of formation, is a siliciclastic continental to coastal sedimentary unit widespread across the Iberian Basin (Aguilar et al., 1971). However, recent works refer to this sedimentary unit with the rank of group owing to its widespread nature and marked diachronism among the different basins of Iberia (i.e., Barrón et al., 2015; Rodríguez-López et al., 2020; Bueno-Cebollada et al., 2021) as the different siliciclastic wedges that constitute the Utrillas Gr may range in age from Albian to Coniacian depending on the geographic region (Gil et al., 2004; Sopeña et al., 2004). In sedimentological terms, the Utrillas Gr has traditionally been interpreted as deposited in fluvial systems (Pardo, 1979). However, this unit has been later reinterpreted as an erg system dominated by aeolian dune deposits in the Maestrazgo and Central domains of the Iberian Basin (i.e., Rodríguez-López et al., 2008, 2013).

In the Cuenca Basin (Fig. 1C), the Utrillas Gr has remained understudied compared to other basins of the IBRS. However, a few research papers dealing with its sedimentology have recently been published, interpreting the deposits as an arid (ephemeral) braidplain system, punctuated by aeolian dune strata, and showing tidal influence towards the upper part of the succession (Chamizo-Borreguero et al., 2016; Bueno-Cebollada and Meléndez, 2018; Bueno-Cebollada et al., 2022). Furthermore, a mid-Albian to earliest Cenomanian age has been assigned to the Utrillas Gr in the Cuenca Basin based on pollen and spore assemblages (Fig. 2; Bueno-Cebollada et al., 2021). In the study area, the deposits of the Utrillas Gr unconformably overlie the coastal to shallow marine deposits of the El Burgal Mb (El Caroch Fm) (Vilas et al., 1982; Meléndez, 1983), which are dated as late Aptian (Bueno-Cebollada et al., 2021). The sedimentary evolution of the Utrillas Gr succession ranging from alluvial deposits towards tide-dominated coastal deposits in the Cuenca Basin indicates a progressive transgressive trend reflecting the Albian to Cenomanian transgression of the Western Tethys in eastern Iberia (Bueno-Cebollada, 2022). The Utrillas Gr succession is sharply overlain by the lower Cenomanian deposits of the Chera Fm (Vilas et al., 1982; Meléndez, 1983; Sopeña et al., 2004). The latter formation consists of green marlstones and mudstones deposited in a shallow marine

environment and precludes the advent of the Upper Cretaceous marine carbonate platforms in the Cuenca Basin.

3. Materials and methods

This paper combines the data of a sedimentary facies analysis and the petrographical, geochemical, and mineralogical study of three exceptionally preserved paleosol sequences (pedocomplexes *sensu* Morrison, 1978; Fedoroff et al., 2010) from the mid-Albian to earliest Cenomanian succession of the Cuenca Basin. Likewise, a thorough literature review on Albian palaeoclimatology from Iberia and neighbouring regions has been carried out to obtain a more accurate picture of the climatic subtleties of the mid-Albian to early Cenomanian time span in Iberia.

The studied exposure (coordinates: 40º07´53.19" N / 1º59´46.46" W) is located in the surroundings of Buenache de la Sierra, Cuenca province, Spain (Fig. 1C). Here, the Utrillas Gr succession crops out in several ravines and extends laterally for almost 1 km. In this sense, Bueno-Cebollada (2022) logged five partial sedimentary sections in the outcrop and included detailed descriptions of the studied section. However, in this work, a combined sedimentary section covering the whole Utrillas Gr succession in the studied locality has been included to simplify and improve comprehension (Fig. 3). The sedimentary section has been constructed using SEDLOG 3.1 (Zervas et al., 2009) in combination with the software Adobe Illustrator CS6 (www.adobe.com). The sedimentological and palaeoedaphological analyses performed in this work are part of the unpublished PhD thesis of the corresponding author of this research paper, CABC (Bueno-Cebollada, 2022).

3.1. Sedimentary facies analysis

The sedimentary facies analysis performed, based on outcrop data, presents a more complete and accurate sedimentological analysis of the mid-Albian to lower Cenomanian succession from the Buenache de la Sierra section than the preliminary study carried out by Bueno-Cebollada and Meléndez (2018). It has been carried out following the guidelines proposed by Collinson

and Thompson (1982), Dabrio and Hernando (2003), and Dalrymple (2010a). In this regard, several parameters have been assessed: lithology, grain size, sedimentary structures, transport directions, morphology of the sedimentary bodies, and biogenic structures. The identified sedimentary facies have been grouped into facies associations (FA) based on their spatial-temporal distribution, and their overall depositional architecture has been analysed (Table I).

3.2. Paleosol analysis methods

Overall, this work presents the study of 10 samples collected from different paleosol horizons of the three studied consecutive paleosol sequences, namely: paleosol 1, 2, and 3, respectively (Fig. 3). The field recognition and outcrop study of the paleosols have been conducted according to Retallack et al. (1988). In the following sections, we detail the different techniques and analyses carried out.

3.2.1. Thin section methodology

Thin sections for the transmitted-light microscope have been prepared, aiming at obtaining new insights into the petrographical structure of the paleosols. The preparation of the 30 μm thin sections has followed the standard procedure for petrographic samples (i.e., Gribble and Hall, 1985; Humphries, 1992). All the thin sections studied in this work have been prepared in the facilities of the Stratigraphy Laboratory of the Facultad de Ciencias Geológicas of the Universidad Complutense de Madrid (UCM), Spain.

3.2.2. Mineralogical analyses methodology

The bulk mineral composition of the paleosol samples has been determined by conducting an X-ray diffraction (XRD) analysis with unoriented powders after grinding and homogenisation of the samples to <53 μm (Table II). The analyses were conducted at Centro de Apoyo a la Investigación (CAI) of the Facultad de Ciencias Geológicas of the Universidad Complutense de Madrid (UCM) with a Bruker D8 Advance diffractometer using Cu-Kα at 30 kV and 40mA, a step size of 0.02 (°2θ), and time per-step of 1s, between 2 and 65 (°2θ). Clay mineral composition was determined on oriented aggregates of the <2 μm fraction obtained by

sedimentation from an aqueous suspension onto glass slides. The oriented aggregates underwent heating (550 °C for 2 hours) and solvation with ethylene glycol (for at least 24 hours), aiming at achieving a more complete characterisation of the clay mineralogy of the samples. A time per-step of 1 s, between 2 and 65 (°2θ), was used in this case. The software DIFFRACplus has been used to acquire, process, and assess the data obtained from the samples. Besides, semi-quantitative analyses were performed following the method proposed by Schultz (1964). The X-ray diffractograms for each of the studied horizons are included in Appendix II.

3.2.3. SEM methodology

The textural and compositional characterisation of the paleosols has been completed with the study of gold-coated chips of selected samples under the scanning electron microscope (SEM). To prepare the samples for the SEM study, small fragments of the samples were collected and dried on a stove at 50 °C for 48 hours. Then, the studied samples were mounted on a specimen holder made of copper and coated in gold. The software EDX Oxford ISIS-Link was used to acquire, process, and appraise the obtained analysis data. The SEM samples were prepared and studied at Centro de Apoyo a la Investigación (CAI) of the Facultad de Ciencias Geológicas of the Universidad Complutense de Madrid (UCM), Spain, using a microscope model JEOL JSM-820 (with microanalysis).

3.2.4. Geochemical analyses methodology

For the geochemical analyses conducted, samples of approximately 100 g of rock were powdered, dried, and sieved to < 53 μm for homogenisation. In each sample, 0.25 g was weighed out and mixed with 0.5 g of flux. Then, the mixture was fluxed and dissolved in HNO_3. Afterwards, the resulting solutions were analysed with ICP-MS (inductively coupled plasma mass spectroscopy) and ICP-OES (inductively coupled plasma optical emission spectroscopy). The measured elements include major elements (SiO_2, Al_2O_3, $Fe2O_3$, CaO, MgO, Na_2O, K_2O, Cr_2O_3, TiO_2, MnO, P_2O_5, SrO, BaO, LOI) and, minor elements and REE (Ba, Co, Cr, Cu, Li, Ni, Sc, Zn, Cs, Ta, Th, Rb, Sr, Nb, Ga, Sn, Hf, U, V, W, Y, Zr, Pb, Ag, As, Cd, Mo, Tl, La, Ce, Pr,

Nd, Sm, Eu, Gd, Tb, Dy, Ho, Er, Tm, Yb, Lu) (Tables III and IV). By convention, major element abundances are expressed as weight percentages of oxides (%) and minor element/REE abundances are expressed as ppm. The geochemical analyses were performed at the ALS Geochemistry facilities in Seville, Spain.

A review of the geochemical methods used in paleosols can be consulted in Retallack (2001) and Sheldon and Tabor (2009), where some of the most useful indexes for provenance and soil chemical processes are referred (Titanium/Alumina, Barium/Strontium, Alumina/Silica, Iron and Magnesium content/Alumina, Silica/Sesquioxides, Alkali/Alumina). All the geochemical ratios used in this study have been calculated by dividing the weight per cent of each oxide or element by its molar mass (g mol^{-1}) (Table V).

Based on the relationship between primary minerals and their secondary products, such as clay minerals, there are other ratios frequently used to measure the degree of chemical weathering in a paleosol (Table VI):

The Chemical Index of Alteration (CIA) (Nesbitt and Young, 1982). It measures the weathering of feldspar minerals and their hydration to form clay minerals.

$$CIA = 100 \times Al_2O_3 / (Al_2O_3+CaO+Na_2O+K_2O)$$

The Chemical Index of Alteration without Potassium (CIA-K). As Potassium is susceptible to diagenesis alteration, Maynard (1992) proposed the CIA-K index.

$$CIA\text{-}K = 100 \times Al_2O_3 / (Al_2O_3+CaO+Na_2O)$$

The Plagioclase Index of Alteration (PIA) (Fedo et al., 1995). It measures the weathering of plagioclases.

$$PIA = 100 \times (Al_2O_3-K_2O) / (Al_2O_3+CaO+Na_2O-K_2O)$$

Bases / Alumina. The CIA and CIA-K focus on the alteration of feldspars; therefore, trying to evaluate other types of minerals, Retallack (2001) proposed this index.

$$(MgO+CaO+Na_2O+K_2O) / Al_2O_3$$

Additionally, using a wide database comprising numerous geochemical analyses, Sheldon et al. (2002) established several mathematical functions that relate chemical weathering indexes with precipitation and average annual temperature. These equations relating CIA-K and Bases to Alumina to precipitation are useful over a 200 – 1600 mm/yr precipitation range.

These functions are:

P1 = 259.34 Ln(B)-759.5; where B is the Bases to Alumina of Retallack (2001). This climofunction has a correlation index of R^2=0,66.

P2= 14.265(CIA-K)-37.632; With an accuracy of R^2=0,73

P3 = $221.12e^{0,0197(CIA-K)}$; with R^2 = 0,72

The functions P1, P2, and P3 have been calculated in this study for two paleosol profiles to estimate the annual palaeorainfall quantitatively.

4. Results

4.1. Sedimentary facies and facies associations

Overall, 12 siliciclastic sedimentary facies have been identified and interpreted in the deposits of the Utrillas Gr in the Buenache de la Sierra section (Appendix I). The studied sedimentary facies have been grouped into four facies associations (FA) which represent different sedimentary environments: proximal alluvial braidplain (FA I), distal alluvial braidplain (FA II), aeolian dunes (FA III), and estuarine to tidally-influenced alluvial deposits (FA I).

4.1.1. FA I: proximal alluvial braidplain

Description: It consists of gravelly and sandy facies, including Gcm, Gt, St, Sp, Sr and Dls (Fig. 4A, B; Table I; Appendix I), and is well represented in the lower part of the studied section (Fig. 3). The FA I is characterised by the occurrence of highly amalgamated lenticular-shaped sandy channelised bodies, which may typically include gravel-dominated deposits (facies Gcm, Gt, and Dls). The sandy bodies are dominated by very coarse grain sizes, and the most commonly observed facies are St and Sp. Cross-bedded sets are abundant in the sand-prone terms of the association, with sets commonly ranging between 20 and 60 cm thick. The palaeocurrents

observed and measured in these sets indicate a S/SE unimodal direction, although SW directions have locally been measured. Additionally, some of the amalgamated channelled bodies may present an upwards gradation into medium to coarse-grained sandstones, dominated by asymmetrical ripples (Sr), showing a reduction in the size of the bedforms. Gravel-dominated facies may be either stratified and lenticular in shape (Gt; Fig. 4A) or massive, lacking any stratification, and with tabular morphologies (Gcm; Fig. 4A, C). Likewise, pebble linings may also be observed as part of this facies association (Dls; Fig. 4B). These pebble linings are flat and sharp surfaces included within the amalgamated sand-dominated bodies that comprise the main component of this facies association. They include faceted pebbles and cobbles with concave polished surfaces.

Interpretation: This facies association presents the coarsest grain sizes of the measured section and represents the proximal sector of a braidplain system. It shows a geometry of stacked amalgamated channels dominated by 2D and 3D subaqueous dunes (facies Sp and St; Table I, Appendix I), lacking overbank deposits. The local occurrence of massive gravel deposits (Gcm) within the channelled bodies is the result of sheet flood events, which consist of sudden surges of coarse sediment due to the reactivation of the alluvial discharge after drier stages (Chamizo-Borreguero et al., 2016).

The presence of faceted pebbles interpreted as ventifacts (Knight, 2008; Rodriguez-López et al., 2010) in this facies association indicates wind reworking of the alluvial deposits during drier stages when the alluvial discharge was minimal or nonexistent. Likewise, deflation lags (Fig. 4B) have been identified within the alluvial deposits that dominate this association. Deflation lags form by intense wind deflation of alluvial deposits in arid settings (Fryberger, 1993). During drier stages, due to the lack of alluvial discharge, wind deflation can blow away the finer particles of sediment, leaving behind a pavement of pebbles-cobble size clasts (Rodriguez-López et al., 2010).

Hence, the FA I is interpreted as the proximal sector of an ephemeral alluvial system whose deposits are reworked by wind action during drier stages giving rise to deflation lags and desert

pavements. The migration of the bedforms is essentially towards the SE/S, which indicates a seawards direction according to previous palaeogeographic reconstructions (Chamizo-Borreguero et al., 2016; Bueno-Cebollada et al., 2021, 2022).

4.1.2. FA II: distal alluvial braidplain

Description: This association mainly comprises sandy and muddy facies (St, Sp, Sr and Fm1) and dominates the middle part of the studied section (Fig. 4D; Table I). This facies association lacks gravelly facies; consequently, the grain size tends to be finer than that of the FA I. Facies St and Sp present the coarser grain sizes and represent the basal terms of the lens-shaped channelled bodies with erosional bases that dominate this facies association. These channelled bodies are commonly overlain by facies Sr and Fm1 (locally, facies Fm2 may also be observed), showing a fining upwards trend. This facies association may present moderate to intense vertical bioturbation primarily developed in facies Fm1, which may affect underlying sand-prone facies. The dominant palaeocurrent directions measured in this facies association are towards the E and SE; however, SW and S directions have been observed locally.

Interpretation: This association is represented by individual sand-prone channelled bodies with basal erosional contacts surrounded by muddy and silty floodplain deposits. As in the FA I, the palaeocurrent directions measured in the channelled sandy facies indicate the seawards migration of the main bedforms. The absence of tidal sedimentary structures and marine ichnofacies suggest that the FA II was deposited landwards from the tidal limit. The alluvial system should have also been a low sinuosity one based on the style of the sedimentary structures observed, mainly due to the lack of inclined heterolithic strata (Ihs), which indicates lateral accretion and is a typical feature of point bars in meandering rivers (i.e., Thomas et al., 1987; Dalrymple and Choi, 2007). Palaeosol development reflects the colonisation of the floodplain areas by plants. This facies association is interpreted as the distal sector of a braidplain alluvial system without tidal influence where gravelly deposits, typical of more proximal areas, are almost absent, and floodplain mudstones and siltstones represent a significant part of the association.

4.1.3. FA III: aeolian dune deposits

Description: This facies association consists of small-scale trough cross-bedded sets of sandstone, and includes two facies (Sae1 and Sae2), characterised by fine- to medium-grained size homometric sandstone (Table I, Appendix I). The sets of cross-bedding generally are 1.5 to 0.5 m thick and extend laterally for more than five meters, depending on the exposure conditions. Foresets of cross-strata within the sets usually dip at high angles (25° to 20°) and lose steepness down-dip towards the bottom sets, displaying moderate to low angles (10° to 5°), eventually down-lapping onto horizontal concave-up bounding surfaces (S; Fig. 4E) which separate sets of cross-bedded strata. These bounding surfaces intersect the underlying cross-bedded sets, producing complex compound cross-bedding styles. These bounding surfaces can also be intersected by higher-rank bounding surfaces (IS), which cut the sandstone bodies defining cosets of cross-strata. The later surfaces are horizontal to sub-horizontal and laterally extensive across the outcrop. Besides, a third type of bounding surface has been identified, representing lower-rank surfaces (R), which are bounded by any of the previously mentioned higher-rank surfaces (S and IS) (Bueno-Cebollada and Meléndez, 2018).

The FA III has been confidently identified in the middle part of the logged succession (Fig. 3), overlying the alluvial deposits of the FA II and displaying, in general, a sharp basal contact, depending on the roughness of the palaeotopography of the underlying deposits. In the studied section, the FA III is sharply overlain by muddy-silty deposits of alluvial origin (FA II) (Fig. 4F).

Interpretation: This facies association is interpreted as compound sets of aeolian dunes, resulting from the migration of primary bedforms, containing smaller wind-laid bedforms migrating faster than the primary ones. Similar aeolian dune architecture has been described by Mountney and Thompson (2002) in the Triassic Helsby Sandstone in the Cheshire Basin (England), referring to this architecture as regularly repeating "small-scale" trough cross-bedding". In this regard, trough-like concave-up surfaces bounding sets of aeolian bedding are interpreted as superimposition surfaces (Kokurek, 1996; Mountney and Thompson, 2002), which are formed

when small bedforms migrate over larger parent aeolian bodies (Mountney, 2004), giving rise to second-order bounding surfaces. A regular recurrence in the occurrence of superimposition surfaces may indicate that bedform migration was taking place under equilibrium conditions (Mountney and Thompson, 2002). Likewise, those major bounding surfaces which define cosets are interpreted as interdune surfaces (Mountney and Thompson, 2002), representing first-order bounding surfaces in aeolian dune accumulations. In the Buenache de la Sierra section, such interdune surfaces represent dry interdunes since they do not present muddy to silty deposits associated. Lower-rank surfaces (R) are interpreted as reactivation surfaces, which are related to airflow fluctuations affecting the lee slope of the dune body (Brookfield, 1977). This can be caused by seasonally induced secondary winds leading to deflation of the lee slopes of the aeolian dune bodies before the main wind resumes (Mountney and Thompson, 2002 and references therein).

The development of aeolian dunes in the Buenache de la Sierra section (Utrillas Gr) has previously been studied by Bueno-Cebollada and Meléndez (2018), who referred to the occurrence of aeolian dunes as a minor sedimentological feature within an arid braidplain system in a transgressive setting. Aeolian dune deposits interacting with ephemeral alluvial braidplain deposits have been reported in the literature in both modern (i.e., Langford, 1989; Krapf et al., 2003; Bullard and McTainsh, 2003) and ancient systems (i.e., Langford and Chan, 1989; Mountney and Thompson, 2002; Mountney and Jagger, 2004; Jordan and Mountney, 2010). Aeolian deposits taking place in arid alluvial settings may accumulate in topographic depressions as a consequence of the aeolian dunes migrating over previous fluvial bedforms (Mountney and Thompson, 2002), giving rise to aeolian pods. In the Buenache de la Sierra section, this sort of aeolian style may be observed (Fig. 4F), where aeolian dune sets infill the irregular topography of the underlying alluvial deposits. Likewise, Chamizo-Borreguero et al. (2016) identified similar aeolian-fluvial interactions, forming aeolian pods in the Uña section (located approximately 10 km to the north of the studied site in this work).

Considering the sedimentary architecture, the aeolian accumulation observed in the Buenache de la Sierra section is interpreted as complex superimposed aeolian dunes with dry interdunes due to the lack of wet interdune deposits interbedded and the presence of dry interdune surfaces (IS) (Bueno-Cebollada and Meléndez, 2018). Additionally, the occurrence of floodplain deposits overlying the aeolian dune deposits in the studied section is the consequence of later flooding of the aeolian deposits by the braidplain system, allowing for plant colonisation (Fig. 4F). In this regard, the lack of incision in the basal contact of the floodplain deposits that overlie the aeolian sandstones is interpreted as a passive rise in the water table (Mountney and Thompson, 2002).

4.1.4. FA IV: inner estuarine

Description: The FA IV is mainly characterised by sandy accumulations that present unidirectional and bidirectional transport directions. The dominant facies observed are St and Sp, representing bedload transport from unidirectional flows. However, the FA IV also includes facies formed from bidirectional flows (Sb1, Sb2). The facies Sb1 consists of sets of cross-bedding, similar to those of facies St and Sp, but displaying opposite palaeocurrent directions (Fig. 4G). The facies Sb2 is typically arranged into deeply incised erosional bodies, which display large-scale trough cross bedding with ripples reworking the lee face of the foresets in the opposite direction from that of the main palaeocurrent (Fig. 4H). More locally, greyish to greenish muddy deposits (Fm1), which can be slightly calcareous and lack bioturbation, have also been identified in this facies association.

Interpretation: Alluvial deposits may be affected by tidal processes even if they are relatively far from the coeval shoreline. In this regard, the identification of tidally influenced alluvial deposits can be an arduous task as the distance upstream increases due to the frequent scarcity of unequivocal diagnostic sedimentary features (i.e., bidirectional flows, double mud drapes, trace fossil or complex compound beddings) to confirm that tidal processes affected alluvial deposits (Shanley et al 1992). However, these diagnostic features are only sometimes sufficiently preserved to be confidently identified in the outcrop. The presence of herringbone-like

structures and trough cross-bedded sets whose foresets are punctuated by rippled sand, suggesting the reworking of the lee faces in a subordinate flow direction, may reflect fluvial currents influenced by ebb and flood tidal currents and/or variations in the alluvial discharge (Shanley et al., 1992; Dalrymple, 2010). Some trace fossils (such as Arenicolites, Skolithos, and Teredolites) found in alluvial strata indicate tidal influence in rivers (Shanley et al., 1992). However, these trace fossils have not been identified in the studied section due to, most likely, the general coarse-grained nature of the studied strata, which hampers their preservation.

Based on the identified facies, this facies association is interpreted as a fluvial-estuarine or coastal plain environment influenced by tidal action, representing the upper part of the Utrillas Gr succession in Buenache de la Sierra. Concretely, the FA IV is interpreted as a sedimentary environment comprising the oscillations between a distal fluvial setting influenced by tides and the upper-middle portion of an estuary or the sandy channels of a coastal plain (Bueno-Cebollada and Meléndez, 2018; Bueno-Cebollada, 2022; Bueno-Cebollada et al., 2022).

4.2. Paleosol outcrop descriptions and petrography

Three representative paleosol profiles have been studied in the field and sampled for subsequent laboratory analyses, consisting of petrographic thin sections, clay mineralogy identification, and whole-rock geochemistry. Field identification of paleosol profiles was based on the presence of vertical structures interpreted as root traces and the differentiation of the profiles into paleosol horizons. The three profiles have common features such as their sandy texture, root traces, presence of sesquioxides and red mottling, and down-profile structuring on different horizons.

The three sequences of paleosols studied in this work are developed in sediments interpreted as the distal alluvial braidplain deposits (FA II; Fig. 3). More concretely, they represent three pedocomplexes (sediment-paleosol sequences; Morrison, 1978) in which the paleosols developed in the associated floodplain deposits and consist of red and purple-mottled mudstones and siltstones. These floodplain deposits overlie alluvial channel deposits and represent their filling, abandonment, and later colonisation by land plants (Bueno-Cebollada, 2022) (Figs. 3, 5).

4.2.1. Paleosol 1

4.2.1.1. Horizon/Sample SB1-A

This horizon is about 40 cm thick and consists of dark yellowish to ochre mudstones and siltstones with scattered sand-sized grains that may present reddish to purple mottling and vertical structures, which seem to indicate the presence of poorly developed roots (Figs. 3, 5B). The lower contact is a sharp contact which shows lateral continuity for 10s of meters. The upper contact is an abrupt and erosional surface corresponding with the base of an overlying fining upwards sandstone body (Fig. 3).

The sample collected in this horizon is dominated by feldspars, monocrystalline quartz, and, to a lesser extent, polycrystalline quartz grains (Fig. 6A). The matrix is dominated by illuvial clay. However, dark brown to black colours are due to the occurrence of small percentages of iron minerals, which precipitated after clay illuviation, impregnating the clayey matrix (Fig. 6B). The sample corresponds to a sandy argillic horizon whose original porosity consisted of simple and continuous pores, which were filled with illuvial clay. The main porosity observed is channel-like elongated structures that tend to branch and taper down and are not filled with illuvial clay or clay coatings (Fig. 6A).

4.2.1.2. Horizon/Sample SB1-B

This horizon is 20 cm thick and consists of light red to reddish mudstones and siltstones slightly mottled with scattered sand-sized grains. The upper contact (with the horizon SB1-A) is sharp, whereas the lower one is gradual, showing lateral continuity for more than 10 meters across the outcrop.

The primary minerals observed in sample SB1-B are monocrystalline quartz and K-feldspar, as well as a smaller number of polycrystalline quartz grains (Fig. 6C). Compared with sample SB1-A, it shows a slightly greater number of quartz grains at the expense of a decrease in K-feldspar grains. The matrix consists of significant amounts of illuvial clay, as in the sample SB1-A, due to the chemical alteration of K-feldspar (Fig. 6D). The dark colour of the matrix is

due to the occurrence of small percentages of iron minerals, which most likely precipitated after clay illuviation, as they impregnated the clayey matrix.

4.2.1.3. Horizon/Sample SB1-C

The horizon is 50 to 60 cm thick and consists of siltstones to very fine-grained sandstones depicting whitish-yellow colours. Locally, and especially towards the upper part of the horizon, some reddish mottling can be observed. The lower contact is diffuse and irregular. The upper contact (with horizon SB1-B) is a gradual and irregular, laterally continuous surface.

The sample corresponding to this horizon, SB1-C, is dominated by quartz and K-feldspars as the main skeletal grains. The quartz grains are mostly monocrystalline, although polycrystalline ones may also be observed. The K-feldspar grains show signs of chemical alteration. In general, the grain size is coarser than those of the overlying horizons SB1-A and SB1-B (Fig. 6E). Regarding the matrix, the amount of clay minerals observed is considerably smaller than that of both overlying horizons. However, small amounts of illuvial clay may still be observed in sample SB1-C (Fig. 6F). The lighter yellowish colour of the illuvial matrix may reflect little iron contents compared to the reddish brown colour observed in the samples SB1-A and SB1-B.

4.2.1.4. Horizon/Sample SB1-D

This horizon is 2 m thick and consists of a coarse-grained arkose sandstone body. The body has a lenticular shape, presenting an erosional base and a fining upwards trend. It may locally contain scattered pebbles, more abundant towards the base. The sample collected at this level corresponds with the upper part of the sandstone body, close to the contact with horizon SB1-C (Fig. 3).

Under the petrographic microscope, the skeletal components of the sample SB1-D are mainly quartz grains (both mono- and polycrystalline) and, to a lesser extent, K-feldspar. The grains of this horizon depict a relatively coarser grain size and a much poorer sorting than those of the overlying horizons (Fig. 6G-H). The main difference with the overlaying horizon SB1-C is the absence of an illuvial clay matrix; consequently, the sample presents a higher primary porosity.

The amount of (illuvial) clay is considerably smaller than that of the overlaying horizon, accumulating around quartz and feldspar grains and forming clay coatings.

4.2.2. Paleosol 2

4.2.2.1. Horizon/Sample SB2-A

The uppermost horizon of the Paleosols 2 is 20 to 30 cm thick and consists of dark reddish mudstones and siltstones which may present a mild purple hue in the outcrop. Mottles are yellow, abundant, and most probably represent small rootlets. The lower contact (with the horizon SB2-B) is gradual to diffuse and shows lateral continuity characterised by a wavy to irregular geometry. Conversely, the upper contact (with an overlying fining upwards coarse-grained sandstone body) is abrupt and erosional (Figs. 3, 5C).

The sample SB2-A, collected in this horizon, is dominated by a groundmass which consists of mainly clay minerals, iron oxides, and hydroxides (Fig. 7A). The skeletal components represent a minor percentage of the horizon and are mainly very fine quartz grains. The groundmass may show alternations between opaque zones dominated by sesquioxides and hydroxides of iron and other zones where birefringent clay minerals are weakly oriented, even not showing a clear preferential orientation in some cases (Fig. 7A). Small mica flakes showing very weak orientation are commonly observed in the sample (Fig. 7B). Ferruginous nodules may develop owing to a moderate impregnation of the clayish matrix with iron oxides.

4.2.2.2. Horizon/Sample SB2-B

This horizon consists of 40 to 60 cm thick greenish-grey to ochre-greenish mudstones with scattered sand-size grains. The mudstones show mottling, although their abundance is relatively low. The lower contact is a sharp one showing lateral continuity for several meters (Figs. 3, 5C). However, its upper contact (with the level SB2-A) is a gradual and diffuse one.

The sample SB2-B, collected in this horizon, is dominated by a clayish matrix, which may locally show impregnations of iron oxides. The main skeletal grains are fine quartz grains (Fig.

7C). The main differences with the overlying horizon (SB2-A) are that quartz grains are slightly more abundant and coarser. Additionally, the horizon SB2-B also shows considerably smaller amounts of iron oxide. The groundmass is dominated by clay minerals in which some ferruginous hypocoatings may be observed (Fig. 7D). The hypocoatings are due to the impregnation of the clayish groundmass with iron oxides and hydroxides (i.e., Hematite and Goethite), and their formation is usually subject to alternations between wet and dry climate conditions (intense seasonal changes) (Bullock et al., 1985). Usually, periods of water saturation are needed to give rise to Fe and Mn mobilisation, whilst periods of drought will produce their accumulation. Ferruginous hypocoatings are usually formed by intense drying, allowing the oxidation of iron minerals.

4.2.2.3. Horizon/Sample SB2-C

This horizon is 40 cm thick and consists of slightly white to pinkish fine-grained sandstone with high mudstone amounts. The lower contact is a diffuse one. The horizon SB2-C overlies a finning upwards cross-bedded sandstone body which represents the non-weathered deposits of an alluvial channel (Bueno-Cebollada and Meléndez, 2018; Bueno-Cebollada, 2022) (Figs. 3, 5A, C).

The sample SB2-C is mainly composed of monocrystalline quartz and K-feldspar grains (as skeletal components). The grain size of the skeletal components is considerably coarser and more poorly sorted than those of the overlying SB2-A and SB2-B horizons. The matrix comprises illuvial clay, formed due to primary illuviation, indicating good drainage conditions. Additionally, there is a lack of iron oxides/hydroxides in this horizon, unlike in the overlying horizons (SB2-A and B).

4.2.3. Paleosol 3

4.2.3.1. Horizon/Sample SB3-A

The horizon SB3-A is a 40 cm thick level that consists of dark red to purple coarse- to medium-grained sandstones with significant mudstone amounts. It presents vertical tapering-down

structures and the occasional occurrence of iron concretions and may locally show a faint yellow mottling. The lower contact of this level is a surface with an irregular lateral continuity, showing undulating pockets. Conversely, the upper contact is an abrupt erosional surface overlain by a non-weathered arkose sandstone body showing abundant trough-cross bedding and a finning upwards trend (Figs. 3, 5A, D).

The sample collected in this horizon (SB3-A) is dominated by monocrystalline quartz grains, although polycrystalline ones are also observed. Similarly, some heavily altered K-feldspar grains can be observed, showing partial alteration to clay minerals. The groundmass of the sample is dominated by a matrix characterised by the absence of interference colours (Fig. 8A) due to the presence of opaque or isotropic minerals such as iron sesquioxides (Bullock et al., 1985). Additionally, the groundmass may locally consist of illuvial clay accumulations which present ferruginous hypo-coatings (Fig. 8B). Both the opaque groundmass and the occurrence of ferruginous hypo-coatings reflect the impregnation of the clayish matrix with iron compounds, which is identified by the presence of red (hematite) and yellow (goethite) colours (Fig. 8C).

4.2.3.2. Horizon/Sample SB3-B

The paleosol horizon SB3-B is 30 cm thick and consists of white coarse- to medium-grained sandstones with significant amounts of mudstone. It presents abundant vertical dark red structures emanating from horizon SB3-A, which branch and taper downwards. These structures reflect an intense root development in the soil (Fig. 5A, D). Additionally, these vertical structures show a drab-haloed mottled appearance, most likely due to the dehydration of yellow and brown ferric oxyhydrates into red hematite during diagenesis (Retallack, 2001). However, according to this author, drab-haloed roots may represent the last plant crops growing in a paleosol before its burial. The lower contact of this level is diffuse to gradual.

The skeletal fraction of the sample SB3-B consists of monocrystalline quartz grains and minor proportions of feldspar. Polycrystalline quartz grains are also observed in smaller amounts (Fig. 8D). The average grain size of this sample is slightly coarser, and the sorting is poorer than that

of the sample SB3-A. The intergranular space is occupied by illuvial clay due to the alteration of the K-feldspar grains. Dark colours in the matrix are due to the occurrence of opaque minerals such as iron sesquioxides similar to those of the sample SB3-A (Fig. 8A).

4.2.3.3. Horizon/Sample SB3-C

This horizon is 120 cm thick and consists of a coarse to very coarse white sandstone body with abundant cm-scale trough-cross bedding showing abundant pebbles towards the base. It is also affected by the same vertical drab-haloed dark red structures observed in horizon SB3-B, interpreted as root traces, tapering downwards for more than a metre. The sample studied in this level (SB3-C) has been collected in one of these downwards tapering structures. The upper contact (with horizon SB3-B) is diffuse to gradual. The lower contact of this level is diffuse and overlies the deposits of a fining upwards coarse-grained sandstone body with an erosional base, interpreted as an alluvial channel (Bueno-Cebollada and Meléndez, 2018; Bueno-Cebollada, 2022) (Figs. 3, 5D). The sample studied in this level (SB3-C) has been collected from one of the dark red downwards tapering structures.

The sample SB3-C shows similarities with the samples SB3-A and SB3-B. It is characterised by abundant quartz grains (mainly monocrystalline) and fewer K-feldspar grains. However, the grain size in this sample tends to be coarser than those of the samples SB3-A and SB3-B (Fig. 8E). The matrix is dominated by an opaque groundmass that is almost ubiquitous. Likewise, abundant accumulations of illuvial clay are observed, which, at times, they may form microlaminated clays with bow-like distribution patterns (Fig. 8F). These crescentic coating fills normally grow among adjacent grains and consist of the alternation of limpid and speckled clay layers. This sort of textural pedofeatures most typically occurs in argillic horizons of soils and paleosols (Bullock et al., 1985).

4.3. Mineralogical characterisation of the paleosols

4.3.1. X-ray diffraction data

4.3.1.1. Paleosol 1

The sample/horizon SB1-A is dominated by clay minerals that account for 72% of the identified minerals. Illite (53%) and kaolinite (43%) are the main clay mineral identified in this horizon. Similarly, a small amount (3%) of mixed-layer illite-smectite (I/S) has also been identified in the sample corresponding to this horizon. To a lesser extent, other minerals such as quartz (18%) and K-feldspar (5%) have been recognised in the analysis together with moderate amounts of the iron oxyhydroxide goethite (6%) (Table II; Fig. 9A). The sample/horizon SB1-B is also characterised by the occurrence of conspicuous percentages of phyllosilicates (72%) dominated by illite and kaolinite, accounting for 37% and 32%, respectively. Small percentages of I/S (3%) are also represented among the identified clay minerals. Quartz, K-feldspar (microcline), and goethite are represented in similar amounts to the horizon SB1-A (Table II; Fig. 9A). The sample/horizon SB1-C is dominated by quartz (43%) and conspicuous percentages of illite and kaolinite (23% and 19%, respectively). Additionally, a higher percentage of microcline (12%) compared to those of the horizons SB1-A and SB1-B (Table II; Fig. 9A). The sample/horizon SB1-D is characterised by the highest percentages of quartz (65%) observed in the paleosol 1 and the lowest percentages of illite and kaolinite (10% and 13%). Regarding K-feldspar, the percentages are similar to those of the horizon SB1-C (Table II; Fig. 9A).

4.3.1.2. Paleosol 2

The sample/horizon SB2-A is dominated by the clay minerals illite and kaolinite (38% and 44%, respectively) with subordinate amounts of I/S (2%) (Table II). Similarly, the percentages of quartz remain relatively high (Fig. 9B). The sample/horizon SB2-B is characterised by high percentages of clay minerals (illite and kaolinite), similar to the ones observed in horizon SB2-A. Conversely, it is worth noting that the percentages of goethite are relatively high, reaching 11% of the overall weight of the sample. Additionally, the analysis reveals a slight drop in the amount of quartz (13%) (Fig. 9B; Table II). The sample/horizon SB2-C presents high contents of clay minerals (74%) dominated by kaolinite (57%) and illite (18%), to a lesser extent.

Similarly, it presents slightly higher percentages of quartz (25%), especially if compared with those of the horizons SB2-A and SB2-B (Fig. 9B; Table II).

4.3.1.3. Paleosol 3

The sample/horizon SB3-A is dominated by clay minerals that represent 69% of the weight of the sample. In this sense, kaolinite is the dominant clay mineral (55%), while the percentage of illite remains comparatively lower (18%). Additionally, goethite presents high percentages, reaching 12% (Fig. 9C; Table II). The sample/horizon SB3-B presents an increase in the percentage of phyllosilicates (77%), characterised by high kaolinite values (~60%) and relatively low ones of illite (Fig. 9C; Table II). The sample/horizon SB3-C is characterised by a slight diminishment in clay minerals compared to horizon SB3-B. In this regard, the percentage of kaolinite is also higher than that of illite. Conversely, the percentage of quartz increases compared to that of horizon SB3-B. Additionally, this horizon shows a conspicuous percentage of goethite, similar to the one observed on the horizon SB3-A (Fig. 9C; Table II).

4.3.2. SEM

In order to obtain a more complete textural and mineral characterisation of the studied samples, Paleosol 1 has been considered for study under the SEM. The reason for only considering this soil profile for the SEM study is its more representative composition that allows illustrating the progressive diminishment in K-feldspar and increase of kaolinite upwards in the soil profile, also observed in the thin sections and XRD analyses.

The sample SB1-D, corresponding to the lowermost sample of the paleosol profile, shows a massive texture with low porosity in which abundant K-feldspar crystals can be identified. Some of these K-feldspar crystals are relatively well-preserved (Fig. 10A), while others are partly altered (Fig. 10B). The K-feldspars crystals are surrounded by kaolinite crystals that form laminar aggregates, giving rise to pseudohexagonal prisms arranged into the classical booklet texture (i.e., Aróstegui et al., 2001) (Fig. 10C, D). The sample SB1-C, located on an upper horizon of the soil profile, shows K-feldspar crystals that are notably more altered and present a

higher porosity developed along cleavage planes, due to the alteration, where small kaolinite crystals grew (Fig. 10E, F). In the sample SB1-B, corresponding to an upper and more altered soil horizon, the porosity is more developed than in the lower horizons of the soil profile and most of the K-feldspar has been altered to kaolinite that may form pseudohexagonal aggregates, occasionally leaving behind some moulds of K-feldspar crystals (Fig. 10G, H).

These progressive variations in the proportion of kaolinite and K-feldspars seem to indicate that both mineral phases are closely related, given their compositional affinity. In this regard, the textural features observed in the SEM images conform with this pattern indicating the formation of authigenic kaolinite owing to the alteration of the feldspars (Fig. 10). Consequently, the SEM images obtained for the paleosol 1 reflect the progressive mineral alteration of sandstones with abundant feldspar crystals giving rise to authigenic kaolinite crystals.

4.4. Paleosol geochemistry

In this study, seven representative samples of Paleosols 1 (samples SB1A to SB1-D) and 3 (samples SB3-A to SB3-C) were prepared for whole-rock analyses and performed by ICP-OES and ICP-MS. Major-element, minor element, and REE determinations are provided in Tables III and IV, respectively. In this regard, Paleosols 1 and 3 have been selected for the geochemical analysis since they present more significant differences in their mineralogical and geochemical compositions.

Based on the studied geochemical data (Tables III and IV), the main differences between the two studied paleosols (1 and 3) can be summarised as follows: from the uppermost (sample SB1-A) to the lowest horizon (SB1-D) of the profile, Paleosol 1 is characterised by high contents of silica (SiO_2), ranging between 62 to 87%. Alumina (Al_2O_3) contents (8 to 22%) are also relatively high in most samples. Iron (Fe_2O_3) contents range from 0.4 to 3.5%, while Sodium (Na_2O) and potassium (K_2O) contents are 0.2 to 0.14 and around 4%, respectively. In this sense, the main trend observed in Paleosol 1 is a progressive decrease in silica at the expense of increasing alumina upwards in the soil profile. Additionally, the amounts of titanium

oxide (TiO_2) are the highest in the uppermost horizons of the paleosol profile (0.7%) and progressively diminish downwards in the paleosol profile, reaching their lowest value (0.13) in the lowermost horizon, SB1-D. Regarding minor elements and REE, the largest contents in the paleosol 1 are those of Ba (345–439 ppm), Rb (118–198 ppm), and Sr (41–70 ppm), which decrease downwards in the paleosol profile. Paleosol 3 shows higher values of Al_2O_3 and Fe_2O_3 than those of Paleosol 1, but lower values of K_2O, BaO, and SrO. The amount of SiO_2 ranges between 63 and 69%, Al_2O_3 from 16 to 20%, Fe_2O_3 from 1 to 10%, and K_2O from 0.24 to 0.38%. In this sense, the most apparent difference with Paleosol 1, is that Paleosol 3 does not show a decrease in silica and an increase in alumina upwards in the soil profile, as can be seen in Paleosol 1 (Table III). LOI (loss on ignition) values are more significant in the uppermost horizon (SB1-A) of Paleosol 1, where they reach 8.17%, and progressively decrease downwards in the paleosol profile up to 1.76% in the lowermost horizon (SB1-D). Conversely, this trend is not observed in Paleosol 3, where LOI values remain higher and more stable throughout the paleosol profile (Table III).

Regarding CIA, Paleosol 1 shows much higher values in the uppermost horizons, reaching up to 80.66% (horizon SB1-A) and progressively decreasing downwards in the soil profile (64.78% in horizon SB1-D). This trend is less noticeable in the estimated CIA-K and PIA values, which remain significantly more stable across the paleosol profile. Conversely, the mentioned trend in CIA values is not observed in Paleosol 3, which shows stable and higher percentages of CIA throughout the paleosol profile (Table VI).

4.5. Interpretation of the paleosol profiles

The soil characteristics and traits assessed in this work (i.e., sandy texture, root traces, presence of sesquioxides and red mottling, and down-profile structuring on different horizons) seem to reflect different maturity degrees among the studied paleosols, indicating that paleosol 1 is the least developed and paleosol 3 the most mature soil.

The paleosol 1 shows a conspicuous and progressive diminishment in clay minerals (kaolinite, illite, and mixed-layer illite-smectite [I/S]) from horizon SB1-A to horizon SB1-D (ranging from 72% to 24%). Conversely, an increase in quartz (and microcline, to a lesser extent) can be observed from horizon SB1-A to horizon SB1-D. Likewise, iron oxyhydroxide (goethite) has been observed in the two uppermost horizons of the paleosol (SB1-A and SB1-B), while it is not present in the two lowermost horizons (SB1-C and SB1-D) (Table II; Fig. 9A). These trends interpreted from the results of the X-ray diffraction analysis can also be observed in thin section (Fig. 6). More concretely, the occurrence of abundant illuvial clay in samples SB1-A and SB1-B, and its progressive diminishment in samples SB1-C and SB1-D at the expense of quartz and K-feldspar reflects a paleosol profile where the K-feldspars are heavily altered into clay minerals (illuvial clay) in its uppermost horizons (SB1-A and SB1-B) (Fig. 6A, B). Conversely, the diminishment in illuvial clay in horizon SB1-C, and especially in horizon SB1-D reflects the gradual transition into less altered horizons of the paleosol, where K-feldspar and quartz grains are progressively less affected by illuviation and hydrolysis processes than in the overlying soil horizons (Fig. 6C, D). This trend of diminishing percentages of clay mineral downwards in the palaesoil profile is in agreement with the observed CIA values (Table V), which reflect the more intense chemical alteration of the K-feldspar and kaolinisation in the uppermost horizons of the paleosol 1. Additionally, the presence of low amounts of iron oxyhydroxides, such as goethite occurring as a cryptocrystalline constituent of the illuvial clay matrix (illite, kaolinite and mixed-layer illite-smectite) of the upper horizons of the paleosol 1 reflects an intense weathering of the soil due to the chemical process of ferrallisation, typical of well-drained tropical soils, whose higher intensity usually coincides with longer periods of soil formation, greater biomass, and stability in a given ecosystem (Nahon, 1991).

The paleosol 2 shows a greater accumulation of clay minerals and a finer grain size than the two other paleosols studied. The main characteristic observed in this paleosol is the gradual increase in kaolinite at the expense of a decrease in illite downwards in the soil profile, indicating that the main chemical weathering process that affected the soil was illuviation (Figs. 7, 9B). The

occurrence of comparatively high contents of goethite as ferruginous hypocoatings in horizon SB2 - B might have been related to periods when the soil remained waterlogged to a certain extent (Bullock et al., 1985).

In general terms, paleosol 3 shows similar characteristics to paleosol 1. However, the percentage of clay minerals and goethite tend to be higher, while quartz and K-feldspar are found in smaller amounts compared to paleosol 1 (Fig. 9). More concretely, paleosol 3 is characterised by very high contents of kaolinite (at the expense of illite and I/S) and moderately high ones of goethite in horizons SB3-A and SB3-C. The complete lack of goethite in horizon SB3-B seems to be related to variabilities in the intensity of the chemical weathering within the horizon since the collected sample was less affected by the red mottling of the root traces (Fig. 5B) than those collected in the other two horizons of this paleosol. This fact also accounts for the relatively constant values of CIA, CIA-K, and PIA across the paleosol 3 profile, particularly if compared to those of the paleosol 1.

The occurrence of sandstone-prone soils with abundant illuvial clay and moderate amounts of iron oxyhydroxide, such as paleosols 1 and 3, indicates the existence of a well-drained substrate under tropical to subtropical conditions during the time of deposition. In this sense, mixed-layer clay minerals (I/S) reflect early stages of alteration in tropical soils, while conspicuous amounts of kaolinite are associated with tropical soils with good drainage conditions, and goethite is typical of leaching processes in tropical soils (Chamley, 1989; Ruffell et al., 2002; Liu et al., 2012).

An increase in kaolinite and goethite together with a diminishment in illite and mixed-layer illite-smectite in paleosol 3 compared to paleosol 1 seem to indicate a more extended period of soil formation in the former and an increase in the biomass and stability of the ecosystem (Bullock et al., 1985; Nahon, 1991). This longer time of soil formation conforms with the field observations as paleosol 3 is pervasively affected by root traces and mottling compared to paleosol 1 (Figs. 5, 6, 8).

Conversely, the more mudstone-prone nature of paleosol 2 suggests that it was subject to more waterlogging or, at least, did not have the well-drained conditions that paleosols 1 and 3 seem to reflect. Therefore, paleosol 2 might have been tentatively related to the muddy floodplain areas of the distal part of an alluvial braidplain system interpreted by previous works (Bueno-Cebollada and Meléndez 2018; Bueno-Cebollada, 2022). Conversely, paleosols 1 and 3 might have developed in more sand-prone substrates, probably related to the abandonment of alluvial channels after they were filled with sediment or the alluvial system migrated.

5. Discussion

5.1. Paleosol classification

In order to classify the type of paleosol into an existing system, Retallack (2001) suggests the US classification system for soils (US Soil Survey Staff, 1999), which is subdivided into 12 orders. Mack et al. (1993) proposed a classification system specifically applied to paleosols. Considering the features of the three paleosol profiles analysed here and their state of development, they have been assigned to the order Spodosols of the Retallack (2001) and Mack et al. (1993) classification systems.

The most superficial horizon of all the profiles shows a higher content of clays, and it is considered an area of accumulation of clays and designated as a B horizon. However, the amount of clays, and the thickness of this horizon, which rarely exceeds 50 cm, prevents its classification as an argilic, Bt, horizon. The abundant vertical red mottling, clay coatings and presence of iron compounds forming opaque and amorphous zones observed in thin sections suggest its classification as a Bs horizon. Therefore, Bs-BC-C is the most plausible structuring of the paleosol profiles 1 and 3 from top to base. Most likely, the subsurface Bs horizon could be considered a spodic horizon, as most spodic horizons are levels in which organic matter, aluminium, and iron accumulated (US Soil Survey Staff, 1999). The amount of organic matter is most easily determined by dry combustion (LOI), following the suggestion of Mack et al. (1993) and references therein. As observed in the whole-rock geochemistry results, B horizons of the profiles show the highest LOI values (around 8%), suggesting higher percentages of

organic matter (Table III). Illuviation of iron, clays, and alumina are interpreted by observation of thin sections and variation of Hydrolysis indexes downwards in the soil profiles (Table V). The identification of the three paleosol profiles as Spodosols is also based on their texture since most Spodosols have few clay-sized phyllosilicates, and their particle-size class is mostly sandy and sandy-skeletal. Spodosols are most extensive in areas of cool, humid, or perhumid climates. However, they also form in hot, humid tropical regions, mainly in quartz-rich sands with good drainage conditions (US Soil Survey Staff, 1999).

The three soils present the same parental material as Ti/Al index does not show significant variations in their profiles, as observed in Table V. As observed in the analyses conducted in this work, the sandy texture of the paleosols is mainly composed of monocrystalline quartz and K-feldspars grains. In this sense, the lower horizons of the studied paleosols are characterised by less weathered minerals, whilst the upper horizons present corroded feldspars and signs of illuviation such as ferruginous hypocoatings and impregnation of the clayish matrix by iron oxides. This fact is particularly conspicuous in the profile of paleosol 1 (Fig. 6). Therefore, it can be interpreted that chemical weathering of the feldspars was produced in situ during the development of the soils. Likewise, the clay mineralogy analysis indicates that the content of kaolinite is higher in the upper horizons of all the studied paleosol profiles, which agrees with the alteration of K-feldspars and the presence of illuviation features observed in thin section and during the SEM study.

In a study on the origin of kaolinite in Lower Cretaceous sedimentary deposits of the Maestrazgo Basin (Oliete Sub-basin, located to the northeast of our study area within the IBRS), Bauluz et al. (2008) described the presence of different types of kaolinites, with two broad categories: low crystallinity kaolinite that constitutes the matrix of claystones and siltstones and was interpreted as detrital, forming after intense weathering of the source area; whereas, different types of high crystallinity kaolinite in sandstones and siltstones were related to in situ growth during incipient diagenesis by K-feldspar dissolution. However, no paleosol profiles were included in their detailed characterisation, and it is somewhat difficult to compare both

sets of samples. Also, in Lower Cretaceous (lower Barremian) sedimentary rocks of the Maestrazgo Basin (Galve Sub-Basin, IBRS), Bauluz et al. (2013) described the early kaolinisation of detrital felspars and micas, followed by diagenetic recrystallisation. They reported the development of paleosols, although they did not attempt to characterise different horizons, and they related the early kaolinisation to the warm and humid conditions described for the Eastern Iberia basin during the early Barremian.

Our results show that, when the relative position within a palaeosol is considered, there is a clear tendency for kaolinite to increase from the lower to the upper horizon at the expense of a concomitant decrease in K-feldspar. This trend is remarkable in palaeosol 1 (Fig. 9) and suggests a mechanism of in situ kaolinisation of K-feldspar as evidenced by the kaolinite particles observed within cleavage planes in the weathered feldspar crystals of the lowest horizon (Fig. 10). The hydrolysis of feldspar and subsequent kaolinite formation would be more pronounced in the heavily illuviated upper horizons. The kaolinite formed through feldspar weathering would probably undergo recrystallisation during incipient diagenesis, especially in sandstones, and this would result in enhanced crystallinity of the kaolinite booklets. Therefore, our results support a mechanism of early kaolinisation and subsequent diagenetic recrystallisation similar to that suggested by Bauluz et al. (2013). However, our interpretation of the palaeoenvironmental conditions, once combined with other independent criteria (sedimentology and palaeobotanical datasets), points towards significant differences, as discussed later in this paper.

Illuviation is associated with hydrolysis, which is the reaction of carbonic acid with a cation-rich mineral grain to produce clay, such as in the case of the hydrolysis of K-feldspar to produce kaolinite. Hydrolysis is interpreted by the high values of the Alumina/Bases, Alumina/Silica and Ba/Sr indices (Table V). The alteration of feldspars into kaolinite is also observed by the high values of the chemical indices of CIA, CIA-K, and PIA in the paleosols 1 and 3 (Table VI). Taking the CIA as an example, if a pure sample of microcline ($KAlSi_3O_8$) is considered, it would have a CIA value of 50. If it were weathered to form pure illite, the CIA value would

increase to 75. Similarly, if the illite were completely leached of potassium and kaolinite formed, the CIA value would further increase up to 100 (Sheldon and Tabor, 2009). In this sense, the CIA values calculated for the upper horizons of the paleosol profiles are very high, reaching 80,66 in Paleosol 1 and 97,68 in Paleosol 3 (Table VI). Consequently, the results obtained from the studied profiles agree with well-drained soils affected by relatively heavy seasonal rains due to the presence of opaque fabrics of iron oxides and hydroxides, high values of chemical indices and alteration of K-feldspars into kaolinite (Retallack, 2001; Sheldon and Tabor, 2009), particularly conspicuous in the uppermost horizons of the paleosols.

Additionally, the estimation of palaeoprecipitation in millimetres of MAP (Mean Annual Precipitation), based on the CIA-K and Bases to Alumina of B horizons of the paleosol profiles, show values between 1047 to 1515 (Paleosol 1) and 1534 and 1564 (Paleosol 3). These palaeoprecipitation values conform with soils of tropical, alternating wet and dry climates (Retallack, 2001). Notwithstanding, it is important to emphasise that the equations used to estimate the palaeoprecipitation (P1, P2, and P3) do not represent very accurate values (Sheldon et al., 2002; Sheldon and Tabor, 2009). Thus, the palaeoprecipitation data obtained here should be analysed together with other palaeoclimate indicators, such as palaeobotanical and sedimentological data, to obtain more accurate results.

5.2. Palaeoenvironmental and palaeoclimatic significance of the paleosols.

The studied paleosols in the Buenache de la Sierra section are developed in the distal part of an ephemeral alluvial braidplain system (FA II; Table I) characterised by multistorey channels and aggradational floodplain mudstones and siltstones that developed close to the palaeocoast, but landwards from the tidal limit (Figs. 3, 5). According to the stratigraphic position within the Utrillas Gr succession, the studied paleosol profiles are most likely considered late Albian in age (Bueno-Cebollada, 2022).

The occurrence of significant amounts of K-feldspar in the lower and less weathered horizons of the studied paleosols (i.e., horizons SB1-C and SB1-D; Table II) and the even higher amounts

of non-weathered alluvial sandstones seem to suggest that the feldspars arrived in this area of the basin in large amounts, indicating a lack or very weak chemical weathering processes in the source areas (or in more proximal areas of the basin). Therefore, it suggests that the pedogenetic alteration of the feldspars into clay minerals took place after they were deposited by the action of mechanical weathering processes in the distal part of the alluvial system.

This seems to indicate the prevalence of arid conditions, more pronounced in proximal areas of the basin where the influence of the Tethys was less intense, which prevented the pervasive chemical weathering of the feldspars. Under these conditions, the sediment would have been transported by the action of ephemeral channels and watercourses that were seasonally active. In this sense, the scarcity of paleosol development, the presence of ventifact pebbles, deflation lags, and aeolian dune development are the main sedimentological features that dominate the Utrillas Gr succession (Chamizo-Borreguero et al., 2016; Bueno-Cebollada and Meléndez, 2018; Bueno-Cebollada, 2022; Bueno-Cebollada et al., 2022) and indicate the prevalence of arid climate conditions in the Cuenca Basin during the mid-Albian to early Cenomanian times. Conversely, the development of paleosols within the studied section reflects the occurrence of shorter-term, more humid periods related to an increase in the rainfall regime. Besides, the intense chemical weathering conditions under which the studied paleosols formed indicate that palaeoprecipitation should have been intense at times. Furthermore, the geochemical analysis of the studied paleosols reveals the occurrence of a seasonal tropical climate with alternating dry and humid seasons/periods, interpreted as that of a tropical savanna ecosystem (Alberts et al., 2015).

The existence of dominantly arid conditions during the mid-Albian to early Cenomanian in the Cuenca Basin is also supported by the palyno- and macroflora presented in Bueno-Cebollada et al. (2021) and Bueno-Cebollada (2022). The palynological assemblages are dominated by large amounts of cheirolepidacean (*Classopollis*) and cupressacean conifer pollen, and low amounts of spores of pteridophyte and pollen of Araucariaceae or Pinaceae affinities (Bueno-Cebollada et al., 2021). Similarly, the mid-Albian to early Cenomanian macrofloras from the Cuenca Basin

are dominated by cupressoid (Cheirolepidiaceae and/or Cupressaceae) conifer taxa characterised by adaptations to water-stress conditions such as *Frenelopsis* and scale-leave conifers (Bueno-Cebollada, 2022). Likewise, the occurrence of similar drought-adapted vegetation, dominated by Cheirolepidiaceae and Cupressaceae conifers, in the neighbouring Maestrazgo Basin during the late Albian has been discussed by Barrón et al. (2023).

In this regard, the marked xerophytic character of the palaeoflora together with the rainfall conditions inferred from the present paleosol analysis seems to indicate an arid climate with a pronounced seasonality, probably characterised by a wet season with monsoon-like rainfall, given the tropical palaeolatitude of Iberia during the "mid"-Cretaceous (25° – 30°N) (i.e., Chumakov et al., 1995; Rodríguez-López et al., 2008, 2010, Burgener et al., 2023). The most plausible climatic model that conforms with these datasets is that of a tropical savanna biome, typically characterised by two distinct seasons regarding rainfall, where the overall amount of evaporation is higher than that of precipitation. Modern tropical savannas differ from other tropical forest ecosystems (i.e., rainforests) in that they have less rainfall (typically around 800 to 1600 mm per year), which is markedly seasonal and typically unforeseeable within seasons (Alberts et al., 2005). However, temperatures tend to be torrid and present slight variations during the year. Consequently, vegetal productivity in the current tropical savanna biome exhibits a marked seasonality driven by rainfall seasonality rather than temperature (Alberts et al., 2005). The modern tropical savanna biome is dominated by plants (grasses, trees, and shrubs) with unique adaptations to thrive under the water-stress conditions of the dry season. These drought adaptations include the development of taproots that reach the water table or trunks that can store water and thick bark capable of withstanding the often occurrence of wildfires (Solbrig, 1996). Similarly, the Cretaceous savanna biomes were characterised by open forests with widely spaced trees dominated by drought-tolerant floras (i.e., *Frenelopsis*, *Pseudofrenelopsis*) and an understorey consisting of ferns, cycadophytes, and, later in the Cretaceous, shrubby angiosperms (Saward, 1992; Halamski et al., 2020). Tropical savannas were relatively common biomes in paratropical and tropical latitudes during the mid-Cretaceous

(Saward, 1992), and during the Albian, the Tropical Savanna climate zone (As/Aw) was widely distributed in low latitudes (Burgener et al., 2023).

Additionally, it should be considered that the high mean temperatures that characterised most of the Cretaceous, particularly the conspicuous episode of global warming that spanned early Albian to Turonian times (i.e., Huber et al., 2002; Wilson et al., 2002; Poulsen et al., 2003; Forster et al., 2007), might have been the driver of very high evaporation rates leading to the marked arid conditions, especially during drier seasons (Haywood et al., 2004). The enhanced evaporation rates during the Albian (76 to 96% more than the modern ones) were probably related to the increased moisture capacity of the warmer Cretaceous atmosphere (Barron et al., 1989) and a vapour holding capacity of 93% greater than the present one (Ufnar et al., 2002).

Therefore, the analysis of the paleosols adds new data to the previous palaeobotany- and sedimentology-based datasets, which has permitted obtaining a more accurate reconstruction of the mid-Albian to earliest Cenomanian palaeoclimate of eastern Iberia. Even though there seems to be an apparent disparity regarding palaeoclimate conditions between the paleosol analysis and the sedimentological and palaeobotanical data, the integration, and comparison of the different datasets suggest the cyclical alternation between a seasonally humid climate and the arid climate that prevailed in eastern Iberia during the studied time span.

5.3. Integration within the framework of the regional palaeoclimate patterns

The mid-Albian to early Cenomanian period has an approximate duration of 8 – 9 Ma (108 – 99 Ma) (Waite et al., 2007; Cohen et al., 2013); therefore, the sedimentation of the Utrillas Gr in the Cuenca Basin might have lasted no more than 8 – 9 Ma or slightly less than that (Bueno-Cebollada et al., 2021). In this sense, the development of paleosols, such as those studied here, reveals climate change periods where the arid climate that dominated eastern Iberia turned into a more seasonally humid tropical savanna climate. Such changes towards more humid climate conditions allowed for the growth of more stable (xeric) woodlands due to the greater water availability as the water table rose.

The cyclical displacement of the low-latitude climatic belts during the mid-Albian to early Cenomanian, as suggested by previous authors (i.e., Chumakov et al., 1995; Hay and Floegel, 2012; Rodríguez-López et al., 2012 Bueno-Cebollada et al., 2021), might account for the development of more humid periods, when palaeosols developed under a tropical savanna climate, and arid periods, when water stress conditions did not allow a more pervasive woodland development in the study area (Fig. 11). In this regard, Skonieczny et al. (2019) and O´Mara et al. (2022) highlight that the precession of the Earth's axis, as it rotates around the sun, leads to changes in the location of the North African monsoon and that these changes have produced the expansion of the savanna biome into the desert landscapes of the Sahara (and vice versa) over 20 ka-cycles during the Pleistocene. Therefore, the mid-Albian to lower Cenomanian succession from the Cuenca Basin provides coherent and well-grounded evidence of these latitudinal changes in the caloric equator, leading to more humid stages when savanna woodlands developed. These changes from an arid climate towards a seasonal tropical climate were repeated cyclically and might conform with the occurrence of 20 ka precession cycles, as suggested by Rodríguez-López et al. (2012) in coeval strata from the neighbouring Central Iberian and Maestrazgo Basins. These authors proposed that wetter periods are interpreted based on the occurrence of hyper-concentrated flows and water-reworked aeolian dune deposits due to higher precipitation rates in the back erg area (Central Iberian Basin), and transition from playa lake systems to coastal and shallow marine deposits in the fore erg area (Maestrazgo Basin). Conversely, drier periods are identified on the basis of aeolian dune and wadi deflation in the back erg, increasing the sand supply towards the distal areas of the basin (fore erg), and the development of desert pavements, indicating a significant slowdown in the hydrological cycle.

Overall, the prevalence of arid conditions in eastern Iberia, as interpreted in this work, conforms with the change towards drier climate conditions, starting in the middle Albian and reaching the early Cenomanian, inferred by previous authors in western Iberia (i.e., Lusitanian Basin) based on changes in clay mineralogy and a conspicuous increase in the xerophyte/hygrophyte ratio of sporomorphs (Berthou et al., 1982; Heimhofer et al., 2012). Likewise, Hochuli (1981) discusses

a change towards more arid conditions during the late Albian in Northern Italy due to the northwards expansion of xerophytic low latitude palynological assemblages with North Gondwanan affinities. Following this line of reasoning, Corentin et al. (2020) infers a semi-arid phase that covers most of the mid-Albian (*D. Niobe* and *D. biplicatus* zones) and presumably the beginning of the late Albian (*D. cristatum* zone) in the Paris and Vocontian Basins in France, whilst in higher palaeolatitudes (i.e., Lower Saxony Basin), the climate should have been significantly more humid (Fenner, 2001). Additionally, Heimhofer et al. (2012) and Corentin et al. (2020) mention a humid phase spanning the early Albian in western Iberia and France. In eastern Iberia, this humid phase coincides with the development of the coal-bearing deposits of the Escucha Fm in the Maestrazgo Basin (i.e., Querol 1990; Rodríguez-López et al., 2009; Álvarez-Parra et al., 2021), and it is not recorded in the Cuenca Basin owing to lack of lower Albian strata in the regional sedimentary record (Bueno-Cebollada et al., 2021). The dominance of more arid conditions in eastern Iberia from the middle Albian is also reflected by the palaeoclimatic reconstructions of Burgener et al. (2023) by the progressive northwards latitudinal expansion of the arid subtropical climates of the northern hemisphere from the Aptian to the Cenomanian (from approximately 15° to 26°N). Such expansion of the arid subtropical climates, particularly across northern Gondwana and eastern Iberia, contrasts with the global increase in humid areas in terrestrial environments from the Hauterivian-Barremian to the Cenomanian times (Burgener et al., 2023). In this sense, the northwards expansion of the NHA belt into eastern Iberia is thought to be related to the development of an Equatorial Humid belt during the Albian (i.e., Rodríguez-López et al., 2012; 2013; 2020). Although, more recent works (Burgener et al., 2023) suggest that the Cretaceous Equatorial Humid belt started developing significantly earlier, during the Hauterivian-Barremian. If this was the case, according to these authors' models, the full latitudinal extent and strength of the Cretaceous Equatorial Humid belt were not reached until the Albian-Cenomanian, with the complete opening of the southern Atlantic, which could have favoured the northwards expansion of the NHA belt into eastern Iberia from the mid-Albian.

In this regard, this mid- to late Albian arid phase should have been stronger in the Cuenca Basin since it was located at a lower palaeolatitude than the Vocontian, Paris, or Lusitanian Basins; and, therefore, more influenced by the NHA belt (Fig. 12). These arid conditions were more intense during the late middle Albian (Heimhofer et al., 2012; Corentin et al., 2020), coinciding with the occurrence of a proximal alluvial braidplain system dominated by ephemeral alluvial deposits, scarcity of paleosols, and palynological assemblages dominated by the genus *Classopollis* in the Cuenca Basin (Bueno-Cebollada et al., 2021; Bueno-Cebollada, 2022). Conversely, a shift towards less arid climate conditions is interpreted during the late Albian in the Cuenca Basin, coinciding with the deposit of the distal alluvial to estuarine succession where the studied paleosols developed. This change to less arid conditions during the late Albian is also observed in coeval strata from Portugal and France (Heimhofer et al., 2012; Corentin et al., 2020) and conforms with the alternation of a tropical savanna climate and the prevailing arid climate in the study area (Fig. 11), reflecting the cyclical expansion and contraction of the NHA and NMH belts in eastern Iberia.

6. Concluding remarks

A combined sedimentary facies and paleosol analysis has been conducted, allowing the characterisation of three late Albian paleosol profiles in the Cuenca Basin (eastern Iberia).

The analysis comprises the study of the Utrillas Gr succession (mid-Albian to earliest Cenomanian) in the Buenache de la Sierra locality (Cuenca Province, Spain) and has permitted us to identify four facies associations that range from proximal alluvial to estuarine deposits: (FA I) proximal alluvial braidplain, (FA II) distal alluvial braidplain, (FA III) aeolian dunes, and (FA IV) inner estuarine. The vertical distribution of the facies associations shows a transgressive trend that reflects the mid-Cretaceous transgression. The results of the sedimentary facies analysis indicate the development of an ephemeral alluvial braidplain system punctuated by aeolian dune deposits that agree with the occurrence of xerophytic taxa in the Cuenca Basin, as previous works indicate.

The three paleosol profiles analysed developed in distal alluvial braidplain deposits (FA II) and are classified as Spodosols based on petrographic, geochemical, and mineralogical datasets. The palaeoedaphological analysis has permitted us to infer that the palaeoclimate during the formation of the late Albian paleosols was tropical, with a marked seasonality regarding palaeoprecipitation. These palaeoclimatic inferences conform with a tropical savanna-type climate (with an estimated palaeoprecipitation ranging from 1000 to 1500 mm per year) and indicate significantly more humid conditions than those previously inferred based on palynological and sedimentological datasets.

To explain this apparent disparity among datasets, we proposed a climatic model rooted in the cyclical latitudinal shifting of the "mid"-Cretaceous climatic belts, giving rise to an alternation of dry and seasonally humid periods during the studied time span. In this regard, the development of paleosols is scarce in the record, representing short time intervals within the Utrillas Gr succession. Therefore, we interpret them as seasonally humid periods, when a savanna climate developed, that alternated cyclically with the prevailing arid climate that characterised eastern Iberia during the mid- and late Albian times. Identifying these periods of increased palaeoprecipitation sheds new light on the late Albian climate of eastern Iberia. More concretely, it reflects that the area was mainly under the influence of the Northern Hot Arid (NHA) belt, but affected by recurrent climatic oscillations during which a tropical savanna climate developed owing to the proximity to the Northern Mid-Latitude Humid (NMH) belt.

This paper is a contribution to the reconstruction of the regional palaeoclimate patterns of the mid-Cretaceous (mid-Albian to earliest Cenomanian) in eastern Iberia, shedding new light on the state-of-the-art knowledge on the topic. Studies such as the present one are a useful tool and contribute to filling gaps in the sedimentary record to improve the accuracy of larger-scale supraregional or global palaeoclimatic reconstructions.

Acknowledgements

This research has been conducted within the framework of the research project CRE (Cretaceous Resin Event: global bioevent of massive resin production at the initial diversification of modern forest ecosystems), funded by the Spanish AEI/FEDER, UE Grant CGL2017-84419. The present manuscript includes part of the results of the corresponding author´s (C.A. Bueno-Cebollada) unpublished PhD thesis. The authors would like to extend their gratitude to the editor, Prof. Dr Howard Falcon-Lang, and an anonymous reviewer for their helpful suggestions that contributed to improving the quality of the manuscript.

References

Aguilar, M.J., Ramírez del Pozo, J., Riba, O., 1971. Algunas precisiones sobre la sedimentación y paleontología del Cretácico inferior en la zona de Utrillas-Villarroya de los Pinares. Estudios Geológicos 27, 497-512.

Alberts, S.C., Altmann, J., Hollister-Smith, J.A., Mututua, R.S., Sayialel, S.N., Muruthi, P.M., Warutere, J.K., 2005. Seasonality and long-term change in a savannah environment. Emergence 16, 17

Allen, J.R., 1963. The classification of cross-stratified units. With notes on their origin. Sedimentology 2, 93-114.

Álvarez-Parra, S., Pérez-De La Fuente, R., Peñalver, E., Barrón, E., Alcalá, L., Pérez-Cano, J., Martín-Closas, C., Trabelsi, K., Meléndez, N., López Del Valle, R., Lozano, R. P., Peris, D., Rodrigo, A., Sarto I Monteys, V., Bueno-Cebollada, C. A., Menor-Salván, C., Philippe, M., Sánchez-García, A., Peña-Kairath, C., Arillo, A., Espílez, E., Mampel, L., Delclòs, X., 2021. Dinosaur bonebed amber from an original swamp forest soil. eLife, 10, e72477

Aróstegui, J., Irabien, M.J., Nieto, F., Sangüesa, J., Zuluaga, M.C., 2001. Microtextures and the origin of muscovite-kaolinite intergrowths in sandstones of the Utrillas Formation, Basque Cantabrian Basin, Spain. Clays and Clay Minerals 49, 529-539.

Arthur, M.A., Dean, W.E., Schlanger, S.O., 1985. Variations in the global carbon cycle during the Cretaceous related to climate, volcanism, and changes in atmospheric CO_2: Natural variations Archean to present, in: Sundquist, E.T., Broecker, W.S. (Eds.), The Carbon Cycle and Atmospheric CO_2. Monographs of the American Geophysical Union 32, pp. 504-529.

Arthur, M.A., Jenkyns, H.C., Brumsack, H.J., Schlanger, S.O., 1990. Stratigraphy, geochemistry, and paleoceanography of organic carbonerich Cretaceous sequences, in: Ginsburg, R.N., Beaudoin, B. (Eds.), Cretaceous Resources, Events and Rhythms: Background and Plans for Research. NATO ASI Series C 304, pp. 75-119.

Aurell, M., Fregenal-Martínez, M., Bádenas B., Muñoz-García, M.B., Élez, J., Meléndez, N., De Santisteban, C., 2019. Middle Jurassic–Early Cretaceous tectono-sedimentary evolution of the southwestern Iberian Basin (central Spain): Major palaeogeographical changes in the geotectonic framework of the Western Tethys. Earth-Science Reviews 199, 1-33.

Barron, E.J., Hay, W.W., Thompson, S., 1989. The hydrologic cycle: A major variable during earth's history. Palaeogeography, Palaeoclimatology, Palaeoecology 75, 157-174.

Barron, E.J., Fawcett, P.J., Peterson, W.H., Pollard, D., Thompson, S.L., 1995. A "simulation" of mid-Cretaceous climate. Paleoceanography 10, 953-962.

Barrón, E., Peyrot, D., Rodríguez-López, J.P., Meléndez, N., López Del Valle, R., Najarro, M., Rosales, I., Comas-Rengifo, M.J., 2015. Palynology of Aptian and upper Albian (Lower Cretaceous) amber-bearing outcrops of the southern margin of the Basque-Cantabrian Basin (northern Spain). Cretaceous Research 52, 292-312.

Barrón, E., Peyrot, D., Bueno-Cebollada, C.A., Kvacek, J., Álvarez-Parra, S., Altolaguirre, Y., Meléndez, N., 2023. Biodiversity of ecosystems in an arid setting: the late Albian plant communities and associated biota from eastern Iberia. PLoS ONE 18, e0282178.

Bauluz, B., Mayayo, M.J., Yuste, A., González López, J.M., 2008. Genesis of kaolinite from Albian sedimentary deposits of the Iberian Range (NE Spain): Analysis by XRD, SEM and TEM. Clay Minerals 43, 459-475.

Bauluz, B., Yuste, A., Mayayo, M.J., Canudo, J.I., 2014. Early kaolinization of detrital Weald facies in the Galve Sub-basin (Central Iberian Chain, north-east Spain) and its relationship to palaeoclimate. Cretaceous Research 50, 214-227.

Berthou, P.Y., Blanc, P., Chamley, H., 1982. Sédimentation argileuse comparée au Crétacé moyen et supérieur dans le bassin occidental portugais et sur la marge voisine (site 398 DSDP): enseignements paléogéographiques et tectoniques. Bulletin de la Société géologique de France 24, 461-72.

Brookfield, M.E., 1977. The origin of bounding surfaces in ancient aeolian sandstones. Sedimentology 24, 303-332.

Bueno-Cebollada C.A., 2022. The sedimentary record of the Albian–Cenomanian transgression in the Cuenca Basin (Iberian Range, Spain): palaeogeographical evolution and palaeoflora (Unpublished PhD thesis). Universidad Complutense de Madrid, Madrid, Spain, 273 pp.

Bueno-Cebollada, C.A., Meléndez, N., 2018. Aeolian dune development in an Albian arid coastal braidplain system in Serranía de Cuenca (Iberian Basin, Spain). Geogaceta 64, 27-30.

Bueno-Cebollada, C.A., Barrón, E., Peyrot, D., Meléndez, N., 2021. Palynostratigraphy and palaeoenvironmental evolution of the Aptian to lower Cenomanian succession in the Serranía de Cuenca (Eastern Spain). Cretaceous Research 128, 104956.

Bueno-Cebollada, C.A., Fregenal-Martínez, M., Meléndez, N., 2022. Along-strike sedimentological variability and architectural patterns of the transgression of a “mid”-Cretaceous braidplain system (Iberian Basin, eastern Spain): A tool for depicting eustatic and tectonic signatures within the framework of a global transgression. Sedimentary Geology 429, 106082.

Bullard, J.E., McTainsh, G.H., 2003. Aeolian-fluvial interactions in dryland environments: examples, concepts and Australia case study. Progress in Physical Geography 27, 471-501.

Bullock, P., Fedoroff, N., Jongerius, A., Stoops, G., Tursina, T., 1985. Handbook for soil thin section description. Waine Research Publications, England, 150 pp.

Burgener, L., Hyland, E., Reich, B.J., Scotese, C., 2023. Cretaceous climates: Mapping paleo-Köppen climatic zones using a Bayesian statistical analysis of lithologic, paleontologic, and geochemical proxies. Palaeogeography, Palaeoclimatology, Palaeoecology, 111373.

Chamizo-Borreguero, M., Meléndez, N., Bermúdez, D.D., Poyato, F. J., 2008. Facies mareales con restos de vertebrados asociadas a un contexto transgresivo: Mb. Calizas de la Bicuerca, (Albiense-Cenomaniense) Serranía de Cuenca, Cuenca Ibérica. Geotemas 10, 195-198.

Chamizo-Borreguero, M., Meléndez, N., De Boer, P.L., 2016. Tidal-bore deposits in incised valleys, Albian, SW Iberian Ranges, Spain. Proceedings of the Tidalites 2012 Conference IAS, 93-115.

Chamley, H. 1989. Clay sedimentology. Springer, Berlin-Heidelberg, 623 pp.

Chumakov, N.M., Zharkov, M.A., Herman, A.B., Doludenko, M.P., Kalandadze, N.N., Lebedev, E.L., Ponomarenko, A.G., Rautian, A.S., 1995. Climatic belts of the mid-Cretaceous time. Stratigraphy and Geological Correlation 3, 42-63.

Cohen, K.M., Finney, S.C., Gibbard, P.L., Fan, J.X., 2013 (updated). The ICS International Chronostratigraphic Chart. Episodes 36, 199-204. http://www.stratigraphy.org/ICSchart/ChronostratChart2021-05.pdf

Collinson, J.D., Thompson, D.B., 1982. Sedimentary Structures. London: George Allen & Unwin, 194 pp.

Corentin, P., Deconinck, J. F., Pellenard, P., Amédro, F., Bruneau, L., Chenot, E., Matrion, B., Huret, E., Landrein, P., 2020. Environmental and climatic controls of the clay mineralogy of Albian deposits in the Paris and Vocontian basins (France). Cretaceous Research 108, 104342.

Dabrio, C.J., Hernando, S., 2003. Estratigrafía. Facultad de Ciencias Geológicas, Universidad Complutense de Madrid, Spain, 382 pp.

Dallmann, W.K., 2015. Geoscience Atlas of Svalbard. KIP Articles 2176

Dalrymple, R.W., 2010a. Interpreting sedimentary successions: facies, facies analysis and facies models, in: James, N.P., Dalrymple, R.W. (Eds.), Facies Models 4. Geological Association of Canada, pp. 3-18.

Dalrymple, R.W., 2010b. Tidal depositional systems, in: James, N.P., Dalrymple, R.W. (Eds.), Facies Models 4. Geological Association of Canada, pp. 201-232.

Dalrymple, R.W., Choi, K., 2007. Morphologic and facies trends through the fluvial–marine transition in tide-dominated depositional systems: a schematic framework for environmental and sequence-stratigraphic interpretation. Earth-Science Reviews 81, 135-174.

Dalrymple, R.W., Zaitlin, B.A., Boyd, R., 1992. Estuarine facies models; conceptual basis and stratigraphic implications. Journal of Sedimentary Research 62, 1130-1146.

Davis, R.A., 2012. Tidal signatures and their preservation potential in stratigraphic sequences, in: Davis, R.A., Dalrymple, R.W. (Eds.), Principles of Tidal Sedimentology. Springer, Dordrecht, pp. 35-55.

De La Horra, R., Benito, M.I., López-Gómez, J., Arche, A., Barrenechea, J.F., Luque, J., 2008. Palaeoenvironmental significance of Late Permian palaeosols in the South-Eastern Iberian Ranges, Spain. Sedimentology 55, 1849-1873.

Fedo, C.M., Nesbitt, H.W., Young, G.M., 1995. Unravelling the effects of potassium metasomatism in sedimentary rocks and paleosols, with implications for paleoweathering conditions and provenance. Geology 23, 921-924.

Fedoroff, N., Courty, M.A., Guo, Z., 2010. Paleosols and relict soils, in: Stoops, G., Marcelino, V., Mees, F. (Eds.), Interpretation of micromorphological features of soils and regoliths, Elsevier, pp. 623-662.

Fenner, J., 2001. Middle and Late Albian geography, oceanography, and climate and the setting of the Kirchrode I and II borehole sites. Palaeogeography, Palaeoclimatology, Palaeoecology 174, 5-32.

Forster, A., Schouten, S., Baas, M., Sinninghe Damsté, J.S., 2007. Mid-Cretaceous (Albian–Santonian) sea surface temperature record of the tropical Atlantic Ocean. Geology 35, 919-922.

Fryberger, S.G., 1993. A review of aeolian bounding surfaces, with examples from the Permian Minnelusa Formation, USA, in: North, C.P., Prosser, D.J. (Eds.), Characterization of Fluvial and Aeolian Reservoirs. Geological Society of America Special Paper 73, 167-197.

Gil, J., Carenas, B., Segura, M., García-Hidalgo, J.F., García, A., 2004. Revisión y correlación de las unidades litoestratigráficas del Cretácico Superior en la región central y oriental de España. Revista de la Sociedad Geológica de España 17, 249-266.

Glennie, K.W., 1970. Desert Sedimentary Environments. Elsevier, Amsterdam.

Gómez, J.J., Aguado, R., Azerêdo, A.C., Cortés, J.E., Duarte, L.V., O'Dogherty, L., da Rocha, R.B., Sandoval, J., 2019. The Late Triassic–Middle Jurassic Passive Margin Stage, in: Quesada, C., Oliveira, J. T. (Eds.), The Geology of Iberia: A Geodynamic Approach. Springer, Cham, pp. 113-167.

Gribble, C.D., Hall, A.D., 1985. A Practical Guide to Optical Mineralogy, London. https://doi.org/10.1007/978-94-011-7804-4

Halamski, A.T., Kvacek, J., Svobodová, M., Durska, E., Hermanova, Z., 2020. Late Cretaceous mega-, meso-, and microfloras from Lower Silesia. Acta Palaeontologica Polonica, 65.

Haq, B.U., 2014. Cretaceous eustasy revisited. Global and Planetary Change 113, 44-58.

Harland, M., Francis, J.E., Brentnall, S.J., Beerling, D.J., 2007. Cretaceous (Albian–Aptian) conifer wood from Northern Hemisphere high latitudes: Forest composition and palaeoclimate. Review of Palaeobotany and Palynology 143, 167-196.

Hay, W.W., Floegel, S., 2012. New thoughts about the Cretaceous climate and oceans. Earth-Science Reviews 115, 262-272.

Haywood, A.M., Valdes, P.J., Markwick, P.J., 2004. Cretaceous (Wealden) climates: a modelling perspective. Cretaceous Research 25, 303-311.

Heimhofer, U., Hochuli, P.A., Burla, S., Oberli, F., Adatte, T., Dinis, J.L., Weissert, H., 2012. Climate and vegetation history of western Portugal inferred from Albian near-shore deposits (Galé Formation, Lusitanian Basin). Geological Magazine 149, 1046-1064.

Hochuli, P.A., 1981. North Gondwanan floral elements in lower to middle Cretaceous sediments of the southern Alps (southern Switzerland, northern Italy). Review of Palaeobotany and Palynology 35, 337-358.

Huber, B.T., Richard D.N., Kenneth G., 2002. Deep-sea paleotemperature record of extreme warmth during the Cretaceous. Geology 30, 123-126.

Humphries, D.W. 1992 The preparation of thin sections of rocks, minerals, and ceramics, Royal Microscopical Society, Microscopy handbooks 24, Oxford, 83 pp.

Jordan, O.D., Mountney, N.P., 2010. Styles of interaction between aeolian, fluvial and shallow marine environments in the Pennsylvanian to Permian lower Cutler beds, south-east Utah, USA. Sedimentology 57, 1357-1385.

Knight, J., 2008. The environmental significance of ventifacts: A critical review. Earth-Science Reviews 86, 89-105.

Kocurek, G.A., 1996. Desert aeolian systems, in: Reading, H.G. (Ed.), Sedimentary Environments: Processes. Facies and Stratigraphy. Blackwell Science, Oxford, pp. 125-153.

Kraus, M.J., 1999. Paleosols in clastic sedimentary rocks: their geologic applications. Earth-Science Reviews 47, 41-70.

Krapf, C.B., Stollhofen, H., Stanistreet, I.G., 2003. Contrasting styles of ephemeral river systems and their interaction with dunes of the Skeleton Coast erg (Namibia). Quaternary International 104, 41-52.

Kvaček, J., 2003. Foliage of a broad-leaved conifer Dammarophyllum from the Cenomanian of Bohemia. Časopis Národního muzea, Řada přírodovědná 172, 13-20.

Kvaček, J., Falcon-Lang, L., Dašková, J., 2005. A new late Cretaceous ginkgoalean reproductive structure *Nehvizdyella* gen. nov. from the Czech Republic and its whole-plant reconstruction. American Journal of Botany 92, 1958-1969.

Langford, R.P., 1989. Fluvial-aeolian interactions: Part I: modern systems. Sedimentology 36, 1023-1035.

Langford, R.P., Chan, M.A., 1989. Fluvial-aeolian interactions: Part II, ancient systems. Sedimentology 36, 1037-1051.

Liu, X., Wanga, Q., Zhang, Q., Feng, Y., Cai, S., 2012. Mineralogical characteristics of the superlarge Quaternary bauxite deposits in Jingxi and Debao counties, western Guangxi, China. Journal of Asian Earth Sciences 52, 53-62.

López-Gómez, J., Alonso-Azcárate, J., Arche, A., Arribas, J., Fernández, J., Borruel-Abadía, V., Bourquin, S., Cadenas, P., Cuevas, P., De la Horra, R., Díez, J., Escudero-Mozo, M.J., Fernández-Viejo, G., Galán-Abellán, B., Galé, C., Gaspar-Escribano, J., Gisbert Aguilar,

J., Gómez-Gras, D., Goy, A., Gretter, N.,Heredia, N., Lago, M., Lloret, J., Luque, J., Márquez, L., Márquez-Aliaga, A., Martín-Algarra, A., Martín-Chivelet, J., Martín-González, F., Marzo, M., Mercedes-Martín, R., Ortí, F., Pérez-López, A., Pérez-Valera, F., Pérez-Valera, J.A., Plasencia, P., Ramos, E., Rodríguez-Méndez, L., Ronchi, A., Salas, R., Sánchez-Fernández, D., Sánchez-Moya, Y., Sopeña, A., Suárez-Rodríguez, A., Tubía, J.M., Ubide, T., Valero, B., Vargas, H., Viseras, C., 2019. Permian-Triassic Rifting Stage (Chapter 3), in: Quesada, C., Oliveira, J. T. (Eds.), The Geology of Iberia: A Geodynamic Approach. Volume 3: The Alpine Cycle. Regional Geology Reviews, Springer, Cham, pp. 29-112.

Mack, G.H., 1992. Paleosols as an indicator of climatic change at the early-late Cretaceous boundary, southwestern New Mexico. Journal of Sedimentary Research 62, 483-494.

Mack, G.H., James, W.C., Monger, H.C., 1993. Classification of paleosols. Geological Society of America Bulletin 105, 129-136.

Marconato, A., de Almeida, R.P., Turra, B.B., dos Santos Fragoso-Cesar, A.R. (2014). Pre-vegetation fluvial floodplains and channel-belts in the Late Neoproterozoic–Cambrian Santa Bárbara group (Southern Brazil). Sedimentary Geology 300, 49-61.

Marfil, R., Callaba, A., Gómez-Gras, D. 1992. Materia orgánica en la Fm. Arenas de Utrillas de Picofrentes (provincia de Soria): diagénesis mineral y orgánica. Geogaceta 12, 43-46.

Martín-Chivelet, J., López-Gómez, J., Aguado, R., Arias, C., Arribas, J., Arribas, M.E., Aurell, M., Bádemas, B., Benito, M.I., Bover-Arnal, T., Casas-Sainz, A., Castro, J.M., Coruña, F., de Gea, G.A., Fornós, J.J., Fregenal-Martínez, M., García-senz, J., Garófano, D., Gelabert, B., Giménez, J., González-Acebrón, L., Guimerà, J., Liesa, C.L., Mas, R., Meléndez, N., Molina, J.M., Muñoz, J.A., Navarrete, R., Nebot, M., Nieto, L.M., Omodeo-Salé, S., Pedrera, A., Peropadre, C., Quijada, I.E., Quijano, M.L., Reolid, M., Robador, A., Rodríguez-López, J.M., Rodríguez-Perea, A., Rosales, I., Ruiz-Ortiz, P.A., Sàbat, F., Salas, R., Soria, A.R., Suárez-González, P., Vilas, L., 2019a. The Late

Jurassic–Early Cretaceous Rifting (Chapter 5), in: Quesada, C., Oliveira, J.T. (Eds.), The Geology of Iberia: A Geodynamic Approach. Volume 3: The Alpine cycle. Regional Geology Reviews, Springer, Cham, 169-249.

Martín-Chivelet, J., Floquet, M., García-Senz, J., Callapez, P.M., López-Mir, B., Muñoz, J.A., Barroso-Barcenilla, F., Segura, M., Soares, A.F., Dinis, P.M., Marques, J.F., Arbués, P., 2019b. Late Cretaceous Post-Rift to Convergence in Iberia (Chapter 7), in: Quesada, C., Oliveira, J.T. (Eds.), The Geology of Iberia: A Geodynamic Approach. Volume 3: The Alpine Cycle. Regional Geology Reviews, Springer, Cham, 285-376.

Maynard, J.B., 1992. Chemistry of modern soils as a guide to interpreting Precambrian paleosols. Journal of Geology 100, 279-289.

Meléndez, N., 1983. El Cretácico de la región de Cañete-Rincón de Ademuz (provincia de Cuenca y Valencia). Seminarios de Estratigrafía 9, 1-242.

Miall, A.D., 1977. A review of the braided river depositional environment. Earth-Science Reviews 13, 1-62.

Miall, A.D., 1978. Lithofacies types and vertical profile models in braided river deposits: a summary, in: Miall, A.D. (Ed.), Fluvial Sedimentology. Canadian Society of Petroleum Geologists, Memoir 5, pp. 597-604.

Miall, A.D., 2010. Alluvial deposits, in: James, N.P., Dalrymple, R.W. (Eds.), Facies Models 4. Geological Association of Canada, pp. 105-138.

Morrison, R.B., 1978. Quaternary soil stratigraphy-concepts, methods and problems, in: Mahaney, M.C., (Ed.), Quaternary soils, York University, pp. 77-108.

Mountney, N.P., 2004. The sedimentary signature of deserts and their response to environmental change. Geology Today 20, 101-106.

Mountney, N.P., Thompson, D.B., 2002. Stratigraphic evolution and preservation of aeolian dune and damp/wet interdune strata: an example from the Triassic Helsby Sandstone Formation, Cheshire Basin, UK. Sedimentology 49, 805-833.

Mountney, N.P., Jagger, A., 2004. Stratigraphic evolution of an aeolian erg margin system: the Permian Cedar Mesa Sandstone, SE Utah, USA. Sedimentology 51, 713-743.

Nahon, D.B., 1991. Self-organization in chemical lateritic weathering. Geoderma 51, 5-13.

Nesbitt, H.W., Young, G.M., 1982. Early Proterozoic climates and plate motions inferred from major element chemistry of lutites. Nature 299, 715.

Norris, R. D., Bice, K. L., Magno, E. A., Wilson, P. A., 2002. Jiggling the tropical thermostat in the Cretaceous hothouse. Geology 30, 299-302.

O'Mara, N.A., Skonieczny, C., McGee, D., Winckler, G., Bory, A. J.M., Bradtmiller, L.I., Malaizé, B., Polissar, P.J., 2022. Pleistocene drivers of Northwest African hydroclimate and vegetation. Nature communications 13, 1-11.

Pardo, G., Villena, J., 1979. Características sedimentológicas y paleogeográficas de la Formación Escucha. Cuadernos de Geología Ibérica 5, 407-418.

Platt, N.H., 1989. Continental sedimentation in an evolving rift basin: the Lower Cretaceous of the western Cameros Basin (northern Spain). Sedimentary Geology 64, 91-109.

Poulsen, C.J., Gendaszek, A.S., Jacob, R.L., 2003. Did the rifting of the Atlantic Ocean cause the Cretaceous thermal maximum?. Geology 31, 115-118.

Pucéat, E., Lécuyer, C., Sheppard, S. M., Dromart, G., Reboulet, S., Grandjean, P., 2003. Thermal evolution of Cretaceous Tethyan marine waters inferred from oxygen isotope composition of fish tooth enamels. Paleoceanography, 18.

Querol, X., 1990. Distribución de la materia mineral y azufre en los carbones de la Formación Escucha. Relación con los factores geológicos, sedimentológicos y diagenéticos. (Unpubl. PhD thesis) Universidad de Barcelona, Spain (in Spanish).

Retallack, G.J., 1988. Field recognition of paleosols. Geological Society of America Special Paper 216, 1-20.

Retallack, G. J., 2001. Soils of the past, third ed. John Wiley and Sons, University of Oregon, Eugene, USA, 552 pp.

Rodríguez, L.R., López, F., Oliveira, J.T., Medialdea, T., Terrinha, P., Matas, J., Martín-Serrano, A., Martín, L.M., Rubio, F., Marín, C., Montes, M., Nozal, F., 2014. Mapa Geológico de España y Portugal 1:1000000. IGME and LNEG.

Rodríguez-López, J.P., Meléndez, N., Boer, P.L.D., Soria, A.R., 2008. Aeolian sand sea development along the mid-Cretaceous western Tethyan margin (Spain): erg sedimentology and palaeoclimate implications. Sedimentology 55, 1253-1292.

Rodríguez-López, J.P., Meléndez, N., Soria, A.R., De Boer, P., 2009. Reinterpretación estratigráfica y sedimentológica de las Formaciones Escucha y Utrillas de la Cordillera Ibérica. Revista de la Sociedad Geológica de España 22, 163-219.

Rodríguez-López, J.P., Meléndez, N., De Boer, P., Soria, A.R., 2010. The action of wind and water in a mid-Cretaceous subtropical erg-margin system close to the Variscan Iberian Massif, Spain. Sedimentology 57, 1315-1356.

Rodríguez-López, J.P., Meléndez, N., De Boer, P.L., Soria, A.R., 2012. Controls on marine–erg margin cycle variability: aeolian–marine interaction in the mid-Cretaceous Iberian Desert System, Spain. Sedimentology 59, 466-501.

Rodríguez-López, J.P., Meléndez, N., de Boer, P.L., Soria, A.R., Liesa, C.L., 2013. Spatial variability of multi-controlled aeolian supersurfaces in central-erg and marine erg-margin systems. Aeolian Research 11, 141-154.

Rodríguez-López, J.P., Peyrot, D., Barrón, E., 2020. Complex sedimentology and palaeohabitats of Holocene coastal deserts, their topographic controls, and analogues for the mid-Cretaceous of northern Iberia. Earth-Science Reviews 201, 103075.

Rubin, D.M., Carter, C.L., 2006. Bedforms and cross-bedding in animation. SEPM Atlas of Sedimentology. SEPM, Tulsa, Oklahoma.

Ruffell, A., McKinley, J.M., Worden, R.H., 2002. Europe Comparison of clay mineral stratigraphy to other proxy palaeoclimate indicators in the Mesozoic of NW Europe. Philosophical Transactions of the Royal Society of London, A 360, 675-693.

Saward, S.A., 1992. A global view of Cretaceous vegetation patterns, in: P.J. McCabe, J.T. Parrish (Eds.), Controls on the Distribution and Quality of Cretaceous Coals, Geological Society of America Special Paper, vol. 267, pp.17-36.

Schultz, L.G., 1964. Quantitative interpretation of mineralogical composition from X-ray and chemical data for Pierre Shale. Professional Papers, United States Geological Survey 391.

Scotese, C.R., 1991. Jurassic and Cretaceous plate tectonic reconstructions. Palaeogeography, Palaeoclimatology, Palaeoecology 87, 493-501.

Scotese, C.R., Gahagan, L.M., Larson, R.L., 1988. Plate tectonic reconstructions of the Cretaceous and Cenozoic ocean basins. Tectonophysics 155, 27-48.

Shanley, K.W., McCabe, P.J., Hettinger, R.D., 1992. Tidal influence in Cretaceous fluvial strata from Utah, USA: a key to sequence stratigraphic interpretation. Sedimentology 39, 905-930.

Sheldon, N.D., Tabor, N.J., 2009. Quantitative paleoenvironmental and paleoclimatic reconstruction using paleosols. Earth-Science Reviews 95, 1-52.

Sheldon, N. D., Retallack, G. J., Tanaka, S., 2002. Geochemical climofunctions from North American soils and application to paleosols across the Eocene-Oligocene boundary in Oregon. The Journal of Geology 110, 687-696.

Skonieczny, C., McGee, D., Winckler, G., Bory, A., Bradtmiller, L.I., Kinsley, C.W., Polissar, P.J., De Pol-Holz, R., Rossignol, L., Malaizé, B., 2019. Monsoon-driven Saharan dust variability over the past 240,000 years. Science advances 5, eaav1887.

Soil Survey Staff, 1999. Soil Taxonomy: A basic system of soil classification for making and interpreting soil surveys, 2nd edition. Agricultural Handbook 436, Natural Resources Conservation Service, USDA, Washington DC, USA, pp. 869

Solbrig, O.T., 1996. The diversity of the savanna ecosystem, in: Solbrig, O.T., Medina, E., Silva, J.F., (Eds.), Biodiversity and savanna ecosystem processes. Springer, Berlin, Heidelberg, pp. 1-27.

Sopeña, A., Gutiérrez-Marco, J.C., Sánchez-Moya, Y., Gómez, J.J., Mas, R., García, A., Lago, M., 2004. Cordillera Ibérica y Costero Catalana, in: Vera, J.A. (Ed.), Geología de España. Sociedad Geológica de España-Instituto Geológico y Minero de España, Madrid, Spain, pp. 465-528.

Spalletti, L.A., Colombo Piñol, F., 2005. From Alluvial Fan to Playa: An Upper Jurassic Ephemeral Fluvial System, Neuquén Basin, Argentina. Gondwana Research 8, 363–383.

Spicer, R.A., Parrish, J.T., 1986. Paleobotanical evidence for cool north polar climates in middle Cretaceous (Albian-Cenomanian) time. Geology 14, 703-706.

Spicer, R.A., Corfield, R.M. 1992. A review of terrestrial and marine climates in the Cretaceous with implications for modelling the 'Greenhouse Earth'. Geological Magazine 129, 169-180.

Thomas, R.G., Smith, D.G., Wood, J.M., Visser, J., Calverley-Range, E.A., Koster, E.H., 1987. Inclined heterolithic stratification—terminology, description, interpretation, and significance. Sedimentary Geology 53, 123-179.

Ufnar, D.F., González, L.A., Ludvigson, G.A., Brenner, R.L., Witzke, B.J., 2002. The mid-Cretaceous water bearer: isotope mass balance quantification of the Albian hydrologic cycle. Palaeogeography, Palaeoclimatology, Palaeoecology 188, 51-71.

Varela, A.N., Yeste, L.M., Viseras, C., García-García, F., Paz, D.M., 2021. Implications of palaeosols in low net-to-gross fluvial architecture reconstruction: Reservoir analogues

from Patagonia and Spain. Palaeogeography, Palaeoclimatology, Palaeoecology 577, 110553.

Vilas, L., Mas, R., García, A., Arias, C., Alonso, A., Meléndez, N., Rincón, R., 1982. La Cordillera Ibérica Suroccidental, in: García, A. (Ed.), El Cretácico de España. Universidad Complutense de Madrid, Madrid, Spain, pp. 457-513.

Waite, L.E., Scott R.W., Kerans, C., 2007. Middle Albian age of the Regional Dense Marker Bed of the Edwards Group, Pawnee Field, south-central Texas. Gulf Coast Association of Geological Societies Transactions 57, 759-774.

Willis, B.J., 2005. Deposits of tide-influenced river deltas, in: Giosan, L., Bhattacharya, J.P. (Eds.) River Deltas–Concepts, Models, and Examples. SEPM special publication 83

Wilson, P.A., Norris, R.D., and Cooper, M.J., 2002, Testing the Cretaceous greenhouse hypothesis using ‘‘glassy’’ foraminiferal calcite from the core of the Turonian tropics on Demerara Rise: Geology 30, 607-610.

Yaalon, D.H., 1971. Soil-forming processes in space and time, in: Yaalon, D.H. (Ed.), Paleopedology–Origin, Nature and Dating of Paleosols. Israel Universities Press, Jerusalem, pp. 29-39.

Yaalon, D.H., 1983. Climate, time, and soil development, in: Wilding, L.P., Smeck, N.E., Hall, G.F. (Eds.), Pedogenesis and Soil Taxonomy. I. Concepts and Interactions. Developments in Soil Science, Volume 11A. Elsevier, Amsterdam, pp. 233-251.

Zervas, D., Nichols, G.J., Hall, R., Smyth, H.R., Luthje, C., Murtagh, F., 2009. SedLog: A shareware program for drawing graphic logs and log data manipulation. Computer and Geosciences 35, 2151-2159.

Ziegler, P.A., 1990. Geological atlas of Western and Central Europe. 2nd ed. 56 enclosures. Shell Internat. Petroleum Maatschappij, The Hague, 239 pp.

Footnotes

Figures:

Fig. 1. (A) Mesozoic basins of the Iberian Peninsula highlighted in green. (IBRS: Iberian Basin Rift System). The extent of the IBRS within Iberia is indicated with a solid red rectangle. Modified after Aurell et al. (2019). (B) Map of the IBRS with its subdivision into basins/domains. The location of the Serranía de Cuenca region within the Cuenca Basin is indicated by a dashed red rectangle. Modified from Fregenal et al. (2017). (C) Simplified geological map of the Serranía de Cuenca region with the location of the studied section (BCH: Buenache de la Sierra) represented by a red star. Modified from Bueno-Cebollada et al. (2021) based on data from the Geological Map of Spain and Portugal (Rodríguez et al., 2014).

Fig. 2. Barremian to early Cenomanian chronostratigraphic chart of the Serranía de Cuenca region (Cuenca Basin). The cart represents a NW-SE (dip section) across the Serranía de Cuenca region. The position of the studied location at the Buenache de la Sierra section is indicated by a blue line. Modified from Bueno-Cebollada et al. (2021).

Fig. 3. Full logged section of the Utrillas Gr in the Buenache de la Sierra (to the left of the figure) where the distribution of the interpreted facies associations has been highlighted in different colours. A close-up and more detailed logged section of the levels where the three studied paleosols are located is included. Modified from an unpublished figure from Bueno-Cebollada (2022).

Fig. 4. (A) Proximal alluvial facies association (FA I). The facies Gcm, Gt, St, and Sp are indicated in the picture. This facies association dominates the lower part of the Utrillas Gr. succession in Buenache de la Sierra (see Fig. 3). (B) Detail of the proximal alluvial facies association (FA I) where the interaction of the facies Dl with the facies St is shown, indicating drier periods with no alluvial discharge in the system. (C) Detail of the facies Gcm, included within the proximal alluvial facies association (FA I). The occurrence of moderately faceted pebbles is indicated in the pictures by white circles. (D) Distal alluvial facies association (FA

II). This facies association is characterised by the occurrence of the low-energy facies Fm1, which may present levels of paleosol development. The FA II occurs in most of the central part of the Utrillas Gr. succession in Buenache de la Sierra (Fig. 3). (E) Detail of an aeolian dune body (FA III), including the facies Sae1 and Sae2. The solid lines represent superimposition surfaces (s). (F) Interaction between aeolian (FA III) and alluvial deposits (FA II). The aeolian deposits overlay alluvial channel deposits and are overlain by mottled overbank deposits. (G) Detail of the facies Sb1, included within the inner estuarine facies association (FA IV), where bedding with opposite bedform migration directions can be observed. (H) Detail of the facies Sb2, included within the FA IV. The large yellow arrow indicates the main palaeocurrent direction and the foreset migration. The smaller white arrows indicate a subordinate palaeocurrent direction reworking the foresets due to tidal action. The hammer for scale in the pictures is approximately 35 cm long. See Table I for description and interpretation of facies associations.

Fig. 5. (A) General view of the studied paleosol succession in Buenache de la Sierra (see Fig. 3). Lateral extension of paleosols SB1, SB2 and SB3 is indicated with white dotted lines. The white elongated triangles indicate the trends in grain/size in each of the studied paleosols. (B, C, and D) Field pictures of Paleosols SB1, SB2 and SB3 with the identified soil horizons bounded by white dotted lines. The dashed white line indicates the upper boundary of the paleosols with the overlying alluvial sandstone body. The measuring stick for the scale in (B) and (C) is 40 cm. Hammer for scale in (C) is approximately 35 cm long. Unpublished figure from Bueno-Cebollada (2022).

Fig. 6. Paleosol SB1 photomicrographs taken under plane-polarised light. (A) Sample SB1-A showing polycrystalline and monocrystalline quartz grains and K-feldspar grains with intense alteration to clay minerals. (B) Close-up of sample SB1-A, where the alteration of the K-feldspar grains can be observed. Due to hydrolysis processes, quartz grains are also partly corroded, showing irregular edges. (C) Sample SB1-B is dominated by altered K-feldspar grains and monocrystalline quartz. The matrix consists of illuvial clay. Channel-like porosities lacking

any infill are most likely due to bioturbation by rootlets. (D) Detail of the partially dissolved K-feldspar grains and the illuvial clay matrix. (E) Sample SB1-C showing abundant mono- and polycrystalline quartz grains and K-feldspar grains. The matrix consists of illuvial clay in proportionally minor quantities than in samples SB1-A and SB1-B. (F) Close-up of the sample SB1-C where an accumulation of illuvial clay can be observed. (G) Sample SB1-D. Note the poor sorting and overall coarser grain size of quartz grains and the lack of clay matrix. (H) Detail of a K-feldspar crystal in the sample SB1-D. Q: quartz; F: feldspar; IC: illuvial clay; P: porosity. Red scale bars in (A, C, E and G) are 1000 µm. Blue scale bars in (B, D, F and H) are 200 µm. Unpublished figure from Bueno-Cebollada (2022).

Fig. 7. Photomicrographs from Paleosol SB2. (A) Sample SB2-A dominated by a groundmass of clay and iron oxides forming ferruginous hypocoatings. (B) Close-up of (A) where the groundmass of clay can be observed together with scattered mica flakes. (C) Sample SB2-B with larger grain sizes and lower quantities of clay matrix than in sample SB2-A. (D) Close-up of sample SB2-B with ferruginous hypocoatings matrix indicated by red arrows. (E) Sample SB2-C showing coarser grain size and poorer sorting of quartz grains compared with overlying horizons SB2-A and SB2-B. (F) Close-up of sample SB2-C. The sample is dominated by quartz grains and abundant illuvial clay and mica flakes. Q: quartz grains; Mi: mica flakes. A, C, E are taken under plane-polarised light and B, D, F under crossed-polarised light. Red scale bars in (A, C, and E) are 1000 µm. Blue scale bars in (B, D, and F) are 200 µm. Unpublished figure from Bueno-Cebollada (2022).

Fig. 8. Photomicrographs of Paleosol SB3. (A) Sample SB3-A showing skeletal components dominated by monocrystalline and, to a lesser extent, polycrystalline quartz grains. The conspicuous dark colour of the fine fraction is composed of iron oxides and hydroxides. (B) Close-up of SB-3-A showing iron hypocoatings of yellowish to dark brown illuvial clays. (C) General view of sample SB3-B showing the skeletal components dominated by quartz grains and a matrix dominated by clay minerals and iron oxides. (D) Close-up of sample SB3-B. The white arrow at the upper central part of the picture indicates dark red impregnations of iron

compounds (such as hematite) in the matrix. Light brownish to yellow-coloured spots (white arrow at the middle left part) of scattered hydrated iron compounds of goethite. (E) Sample SB3-C dominated by quartz (poly- and monocrystalline) and K-feldspar grains with a matrix of illuvial clay. (F) Close-up of sample SB3-C where red arrows indicate locations of micro-laminated illuvial clays. A, B, C, D, and F are taken under plane-polarised light, and E under crossed-polarised light. Red scale bars (A, D, and E) are 1000 µm. Blue scale bars (B, D, F and H) are 200 µm. Unpublished figure from Bueno-Cebollada (2022).

Fig. 9. Mineral compositions of the studied paleosol profiles of Arenache de la Sierra. Y-axis represents the percentage value of the different minerals identified in the X-ray diffraction analysis of the sampled horizons (X-axis). (A) Paleosol SB1; (B) Paleosol SB2; (C) Paleosol SB3. Unpublished figure from Bueno-Cebollada (2022).

Fig. 10. Images of paleosol SB1 under the scanning electron microscope (SEM): (A) Microcline (K-feldspar) grain showing a low alteration degree in the sample SB1-D. (B) Example of another microcline crystal from the same sample (SB1-D) being slightly more altered than that of A. (C) and (D) hexagonal laminae aggregates of kaolinite (Kaol) forming prisms with the typical "booklet" texture in sample SB1-D. (E) Detail of sample SB1-C showing a microcline (K feld) crystal partially altered following parallel planes in which thin kaolinite laminae (Kaol) develop. Kaolinite laminae are indicated by an arrow. (F) Small crystal of microcline in sample SC1-C showing a more intense alteration than that of E. (G) Example of sample SB1-B where a few moulds of K-feldspar crystals can be seen (white arrow). The feldspars have been practically replaced by kaolinite. (H) General aspect of the sample SB1-B showing a texture dominated by clay minerals where kaolinite crystals prevail. Unpublished figure from Bueno-Cebollada (2022).

Fig. 11. Schematic 3D models of the mid-Albian to earliest Cenomanian alluvial braidplain system interpreted for the Cuenca Basin. (A) Representation of the arid periods when the Cuenca Basin was under the influence of the NHA belt. (B) Representation of the seasonally humid periods when the Cuenca Basin was under the influence of the NWM belt. The source

areas towards the NW (Iberian Massif), the Tethys coast towards the SE, and the schematic distribution of the studied facies associations are also represented. In addition to the savanna woodlands, the tentative distribution of coastal halophytic vegetation is represented in the models after Bueno-Cebollada (2022) and Barrón et al. (2023).

Fig. 12. (A) Schematic palaeogeographical reconstruction of western Europe during the late Albian with the location of the Cuenca Basin (*CB*) in Iberia and the areas under the influence of the North-Latitude Hot Arid Belt (NHA Belt) and Mid-Latitude Warm Humid Belt (MWH Belt). The two-sided arrow symbol represents the northwards and southwards oscillations of the boundary between both climate belts (red dotted line). The position of compared localities from previous works is also included (*MB*: Maestrazgo Basin; *LB*: Lusitanian Basin; *VB*: Vocontian Basin; *APB*: Ardennes-Paris Basin; *LSB*: Lower Saxony Basin; *SA*: Southern Alps region). IB: Iberian Massif; ACM: Armorican-Central Massif; AN: Anglia; AF: Africa; RBM: Rhine-Bohemian Massif; FS: Fennoscandian Shield. (B) The summary table indicates the proxies (Mineralogical/Geochemical, Sedimentological, or Palaeobotanical) used by previous authors in the compared localities and the Cuenca Basin. The figure is based on palaeogeographical data from Scotese et al. (1988), Ziegler (1990), Scotese (1991), Corentin et al. (2020), and Burgener et al. (2023).

Tables:

Table I. Summary of the four facies associations (FA I – FA IV) identified by Bueno-Cebollada (2022) in the Buenache de la Sierra section. For more details on the sedimentary facies analysis, see Appendix I, where the identified facies that constitute the facies associations are described and interpreted.

Table II. Mineralogical composition of the studied paleosols samples obtained from X-ray diffraction data (see Appendix II for the diffractograms). The abundances are expressed in weight percentages (%).

Table III. Major-elements data obtained from Paleosols SB1 and SB3. LOI: loss on ignition.

Table IV. Minor-elements and REE data obtained from Paleosols SB1 and SB3.

Table V. Indexes used to evaluate pedogenesis and provenance of parental material for Paleosols SB1 and SB3.

Table VI. Indexes used to evaluate chemical weathering and estimate of palaeoprecipitation in millimetres of MAP (Mean Annual Precipitation) for Paleosols SB1 and SB3. See the text for the formula used to obtain palaeoprecipitation P1, P2, and P3. The palaeoprecipitation has only been estimated for B horizons as indicated by Sheldon and Tabor (2009).

Appendixes:

Appendix I. Sedimentary facies table including the 12 facies identified and their forming processes and environments.

Appendix II. Diffractograms of the studied paleosol horizons.

Facies association	***Facies***	***Interpretation***	***References***
FA I: Proximal alluvial	*Gcm, Gt, St, Sp, Sr, Dl*	Ephemeral alluvial/braidplain environment (proximal zone).	Miall (1977, 2010); Bristow and Best (1993); Rodríguez-López et al. (2010).
FA II: Distal alluvial	*St, Sp, Sr, Fm1, Fm2, Dl*	Ephemeral alluvial/braidplain deposits (distal zone). Landwards from the limit of tidal influence.	Miall (1977, 2010); Bristow and Best (1993); Chamizo-Borreguero et al. (2016).
FA III: Aeolian dunes	*Sae1, Sae 2*	Aeolian dunes associated with the ephemeral alluvial setting.	Mountney and Thompson (2002); Rodríguez-López et al. (2008); Bueno-Cebollada and Meléndez (2018).
FA IV: Inner estuarine	*Sb1, Sb2, St, Sp, Sr, Fm2*	Proximal estuarine setting within the supratidal to the upper intertidal zone.	Dalrymple (2010b); Daidu (2012); Chamizo-Borreguero et al. (2016).

Sample	Quartz	Microcline	Goethite	Illite	Kaolinite	I/S
SB1A	18	5	6	38	31	3
SB1B	18	5	5	37	32	3
SB1C	43	12	0	23	19	3
SB1D	65	11	0	10	13	1
SB2A	17	0	0	38	44	2
SB2B	13	1	11	35	40	0
SB2C	25	1	0	18	57	0
SB3A	18	1	12	14	55	0
SB3B	23	0	0	17	60	0
SB3C	28	1	11	13	48	0

Sample	SiO2	Al2O3	Fe2O3	CaO	MgO	Na2O	K2O	Cr2O3	TiO2	MnO	P2O5	SrO	BaO	LOI	Total
	%	%	%	%	%	%	%	%	%	%	%	%	%	%	%
SB1-A	61,9	21,8	3,43	0,15	0,61	0,21	4,41	0,01	0,71	0,01	0,06	0,01	0,05	8,17	101,49
SB1-B	65,3	20,2	3,32	0,15	0,51	0,18	4,42	0,007	0,63	0,01	0,04	0,01	0,04	6,69	101,49
SB1-C	78,5	12,95	0,85	0,07	0,25	0,16	4,95	0,003	0,27	0,01	0,04	0,01	0,05	3,52	101,61
SB1-D	86,9	8,29	0,37	0,04	0,09	0,14	3,93	0,002	0,13	0,01	0,02	0,01	0,04	1,76	101,71
SB3-A	63,2	17,4	8,73	0,14	0,16	0,04	6,20	0,016	0,91	0,01	0,02	0,01	0,01	8,26	99,15
SB3-B	69,2	20,2	1,14	0,14	0,14	0,04	8,30	0,01	0,42	0,01	0,01	0,01	0,01	8,42	100,07
SB3-C	66	16,8	9,78	0,09	0,13	0,03	4,20	0,008	0,33	0,01	0,06	0,01	0,01	7,27	100,72

Sample	Ba	Co	Cr	Cu	Li	Ni	Sc	Zn	Cs	Ta	Th	Rb	Sr	Nb	Ga	Sn	Hf	U	V	W	Y
	ppm	ppm	ppm	ppm	ppm	ppm	ppm	ppm	ppm	ppm	ppm	ppm	ppm	ppm	ppm	ppm	ppm	ppm	ppm	ppm	ppm
SB1-A	40	8	60	10	40	19	16	34	16,2	1,7	19,9	19 8,5	70 ,3	19,3	34,6	12	6,6	3,89	82	6	45,3
SB1-B	41	5	50	7	30	11	10	20	14,7	4,5	18,55	18 2,5	60 ,2	19,3	29,4	10	5,6	3,8	67	5	48,5
SB1-C	43	1	20	3	20	5	6	13	7,14	0,6	9,08	17 0	50 ,8	16 5,9	,7	6	3,1	1,97	27	1	22,7
SB1-D	34	1	10	2	10	4	3	7	3,61	0,1	11 5,5	41 8	,6	9, 2,7	8	3	1,9	1,64	12	1	15,3
SB3-A	54	15	12 0	19	70	50	10	18	1,73	1,4	24,6	11, 8	25 ,8	16, 6	27	6	10 ,5	3,84	17 5	5	38,9
SB3-B	80	4	70	4	70	14	8	9	1,94	0,6	8,6 3	16, 1	34 ,1	23 8	,7	6	3,1	1,15	22	2	18,4
SB3-C	71	42	60	4	50	23	11	11	1,48	0,4	22	13, 8	64 ,1	19 6,1	6	6	2,1	3,34	14 3	1	18,1

Sample	Zr	Pb	Ag	As	Cd	Mo	Tl	La	Ce	Pr	Nd	Sm	Eu	Gd	Tb	Dy	Ho	Er	Tm	Yb	Lu
	ppm	ppm	ppm	ppm	ppm	ppm	ppm	ppm	ppm	ppm	ppm	ppm	ppm	ppm	ppm	ppm	ppm	ppm	ppm	ppm	ppm
SB1-A	23 0	25	<0 .5	<5	<0 .5	<1	<1 0	43 ,8	92 ,2	12, 05	47, 3	11, 1	2, 07	10, 15	1, 69	8,3 9	1, 59	4, 48	0, 61	4, 16	0, 53
SB1-B	21 1	25	<0 .5	<5	<0 .5	<1	<1 0	41 ,2	99	14, 65	67, 7	17, 55	3, 13	14, 05	2, 05	10, 95	1, 76	4, 93	0, 53	3, 65	0, 59
SB1-C	10 5	27	<0 .5	<5	<0 .5	<1 1	<1 0	21 ,3	44 ,6	5,9 0	26, 1	5,4 7	1, 14	5,4	0, 77	4,3 8	0, 83	2, 59	0, 29	1, 85	0, 26
SB1-D	67	24	<0 .5	<5	<0 .5	<1	<1 0	15 9	24 6	4,0 4	17, 5	3,8 6	0, 75	3,1 2	0, 51	2,7 1	0, 5	1, 66	0, 24	1, 38	0, 21
SB3-A	36 8	12	<0 .5	23	<0 .5	1	<1 0	19 ,2	30 ,7	3,4 9	13	3,4 5	0, 73	4,3 4	0, 92	6,3 4	1, 39	4, 39	0, 71	4, 54	0, 69
SB3-B	10 2	45	<0 .5	<5	<0 .5	<1	<1 0	33 ,1	41 ,1	3,5 7	9,9	1,8 5	0, 34	2,1 4	0, 48	2,9 7	0, 61	1, 88	0, 27	1, 76	0, 28
SB3-C	77	63	<0 .5	6	<0 .5	<1	<1 0	14 7	22 9	17, 9	43, 5	5,3 8	0, 77	3,7 9	0, 6	3,3 5	0, 68	1, 79	0, 23	1, 8	0, 22

Sample	Provenance	Hydrolysis			Oxidation	Hydration	Salinisation
	Titanium / Alumina	Alumina / Bases	Barium / Strontium	Alumina / Silica	Iron+Magnesium / Alumina	Silica / sesquioxides	Alkali / Alumina
SB1-A	0,041	80,66	3,63	0,21	0,17	4,38	0,23
SB1-B	0,040	79,36	4,36	0,18	0,17	4,97	0,25
SB1-C	0,027	69,62	5,51	0,10	0,09	9,87	0,43
SB1-D	0,020	64,78	5,29	0,06	0,06	17,30	0,54
SB3-A	0,067	97,68	1,34	0,16	0,34	4,67	0,02
SB3-B	0,027	97,38	1,51	0,17	0,05	5,61	0,02
SB3-C	0,025	98,09	0,71	0,15	0,39	4,86	0,02

Sample	Chemical weathering			Palaeoprecipitation		
	CIA	CIA-K	PIA	P1	P2	P3
SB1-A	80,66	97,96	97,40	1057,39	1359,73	1522,21
SB1-B	79,36	97,73	97,04	1047,21	1356,46	1515,36
SB1-C	69,62	97,79	96,28	942,44	1357,30	1517,11
SB1-D	64,78	97,02	94,07	-	-	-
SB3-A	97,68	99,25	99,24	1498,01	1378,16	1561,45
SB3-B	97,38	99,35	99,34	1534,74	1379,63	1564,64
SB3-C	98,09	99,60	99,60	1573,55	1383,18	1572,32

Declaration of interests

☒The authors declare that they have no known competing financial interests or personal relationships that could have appeared to influence the work reported in this paper.

☐The authors declare the following financial interests/personal relationships which may be considered as potential competing interests:

HIGHLIGHTS

- Sedimentology and palaeoedaphology study of the Utrillas Group in the Cuenca Basin
- Short-term climatic oscillations in Iberia during the mid-Albian–early Cenomanian
- Cyclical changes from an arid climate to a seasonally dry tropical climate
- New insights on the mid-Cretaceous palaeoclimate of the basins of Eastern Iberia

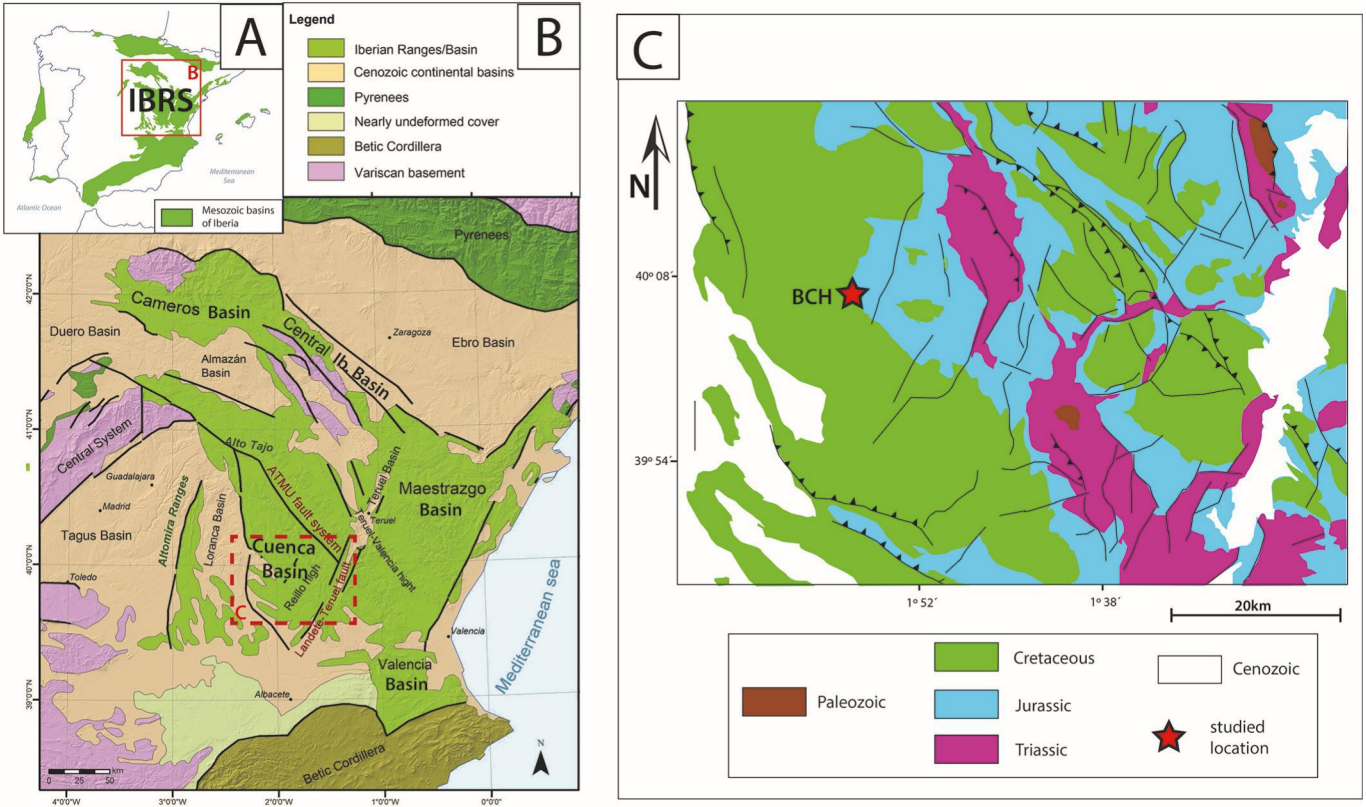
A
B
IBRS
Mediterranean Sea
Atlantic Ocean
Mesozoic basins of Iberia
Legend
Iberian Ranges/Basin
Cenozoic continental basins
Pyrenees
Nearly undeformed cover
Betic Cordillera
Variscan basement
Pyrenees
Cameros Basin
Duero Basin
Almazán Basin
Central Ib. Basin
Ebro Basin
Zaragoza
Central System
Alto Tajo
ATMU fault system
Teruel Basin
Maestrazgo Basin
Guadalajara
Madrid
Tagus Basin
Altomira Ranges
Lorca Basin
Teruel
Toledo
Cuenca Basin
Reillo high
Landete-Teruel Fault
Serrania-Valencia Hight
Valencia
Mediterranean sea
Valencia Basin
Albacete
Betic Cordillera
C
N
0 25 50 km
4°0'0"W
3°0'0"W
2°0'0"W
1°0'0"W
0°0'0"
42°0'0"N
41°0'0"N
40°0'0"N
38°0'0"N
C
N
40° 08´
39° 54´
BCH
1° 52´
1° 38´
20km
Paleozoic
Cretaceous
Jurassic
Triassic
Cenozoic
studied location

Figure 1

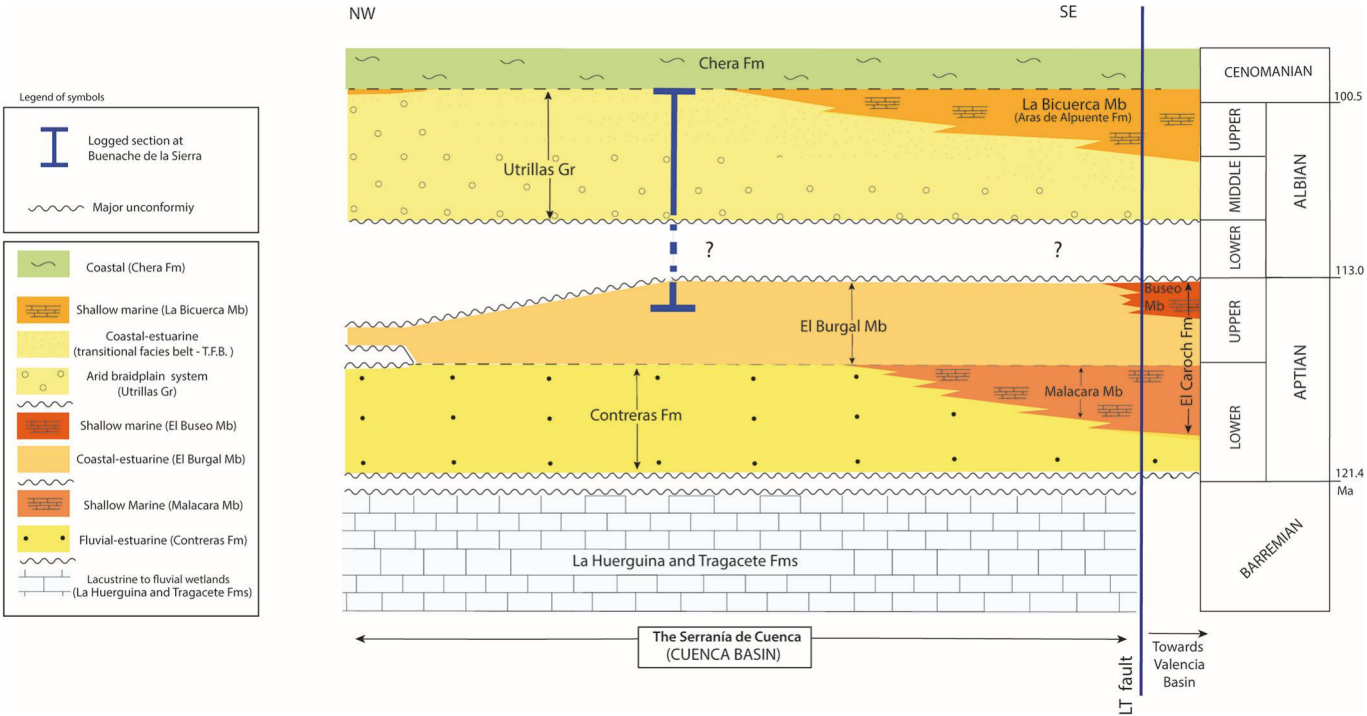
Legend of symbols
Logged section at Buenache de la Sierra
Major unconformiy
Coastal (Chera Fm)
Shallow marine (La Bicuerca Mb)
Coastal-estuarine (transitional facies belt - T.F.B.)
Arid braidplain system (Utrillas Gr)
Shallow marine (El Buseo Mb)
Coastal-estuarine (El Burgal Mb)
Shallow Marine (Malacara Mb)
Fluvial-estuarine (Contreras Fm)
Lacustrine to fluvial wetlands (La Huerguina and Tragacete Fms)
NW
SE
Chera Fm
La Bicuerca Mb
(Aras de Alpuente Fm)
Utrillas Gr
?
?
El Burgal Mb
Buseo Mb
El Caroch Fm
Malacara Mb
Contreras Fm
La Huerguina and Tragacete Fms
The Serranía de Cuenca
(CUENCA BASIN)
LT fault
Towards Valencia Basin
CENOMANIAN
100.5
UPPER
MIDDLE
LOWER
ALBIAN
113.0
UPPER
LOWER
APTIAN
121.4
Ma
BARREMIAN

Figure 2

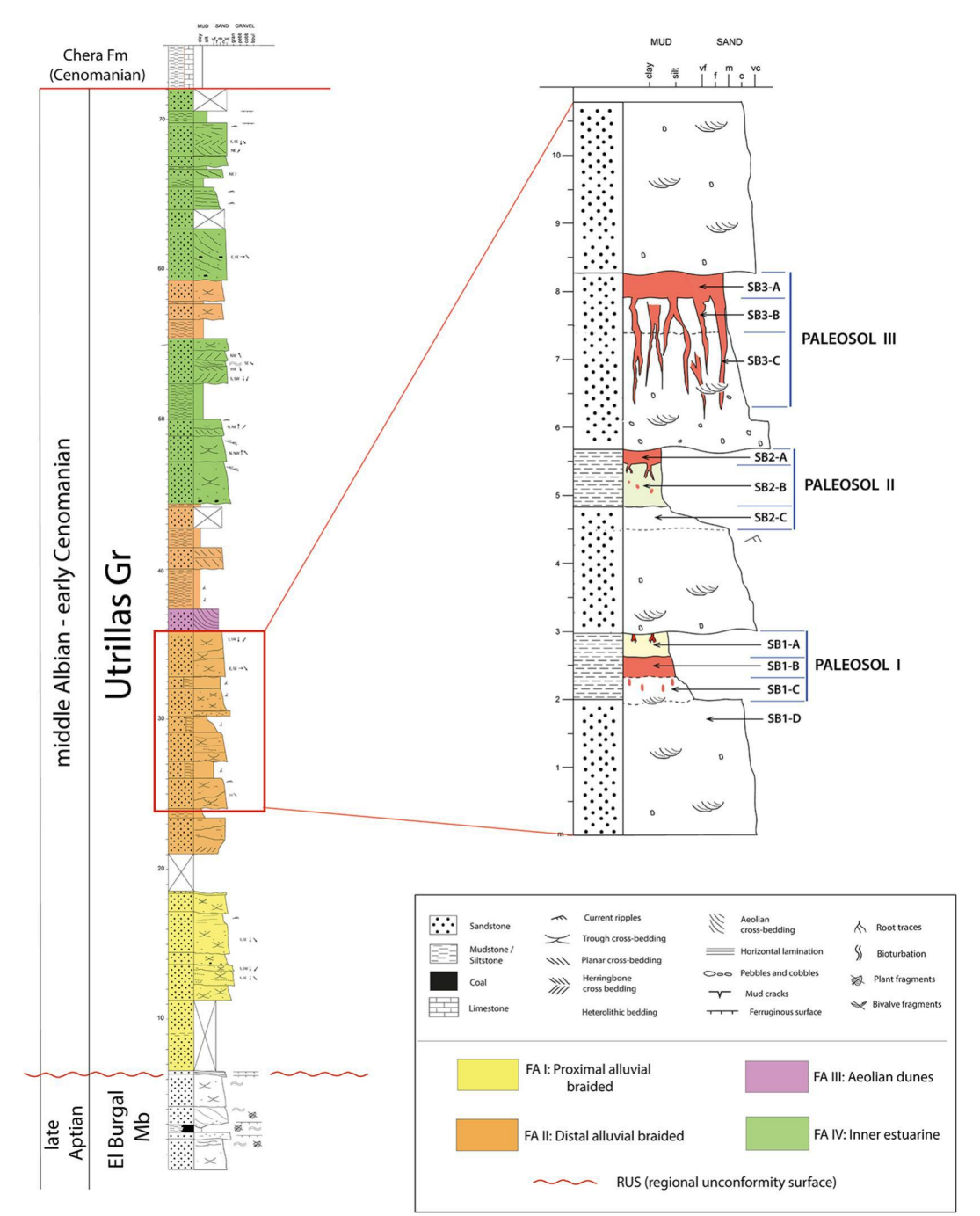
Chera Fm
(Cenomanian)
middle Albian - early Cenomanian
Utrillas Gr
late
Aptian
El Burgal
Mb
MUD
SAND
clay
silt
vf
f
m
c
vc
SB3-A
SB3-B
SB3-C
PALEOSOL III
SB2-A
SB2-B
SB2-C
PALEOSOL II
SB1-A
SB1-B
SB1-C
SB1-D
PALEOSOL I
Sandstone
Mudstone / Siltstone
Coal
Limestone
Current ripples
Trough cross-bedding
Planar cross-bedding
Herringbone cross bedding
Heterolithic bedding
Aeolian cross-bedding
Horizontal lamination
Pebbles and cobbles
Mud cracks
Ferruginous surface
Root traces
Bioturbation
Plant fragments
Bivalve fragments
FA I: Proximal alluvial braided
FA II: Distal alluvial braided
FA III: Aeolian dunes
FA IV: Inner estuarine
RUS (regional unconformity surface)

Figure 3

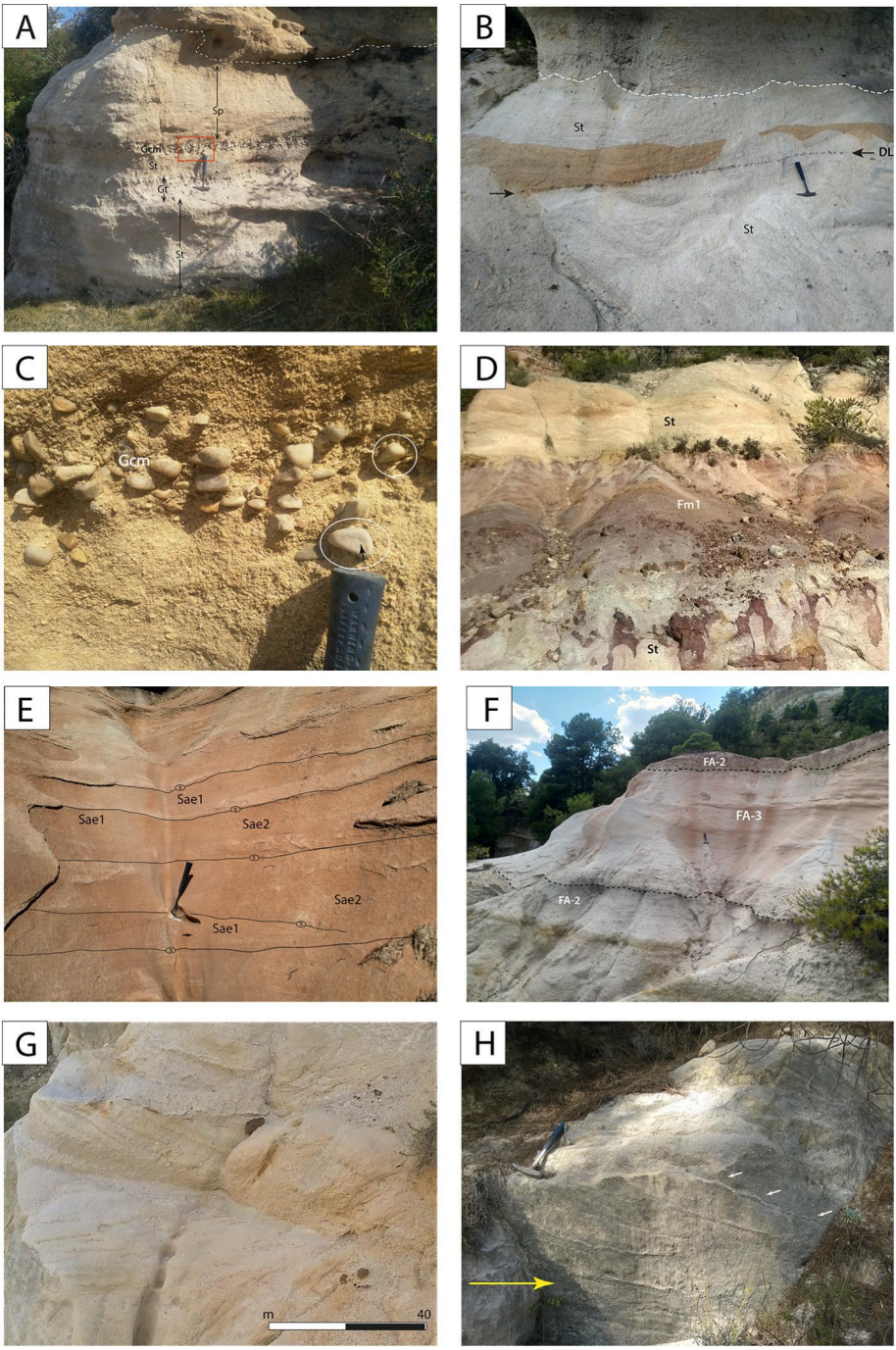
A
Sp
Gcm
St
Gf
St
B
St
DL
St
C
Gcm
D
St
Fm1
St
E
Sae1
Sae1
Sae2
Sae2
Sae1
F
FA-2
FA-3
FA-2
G
m
40
H

Figure 4

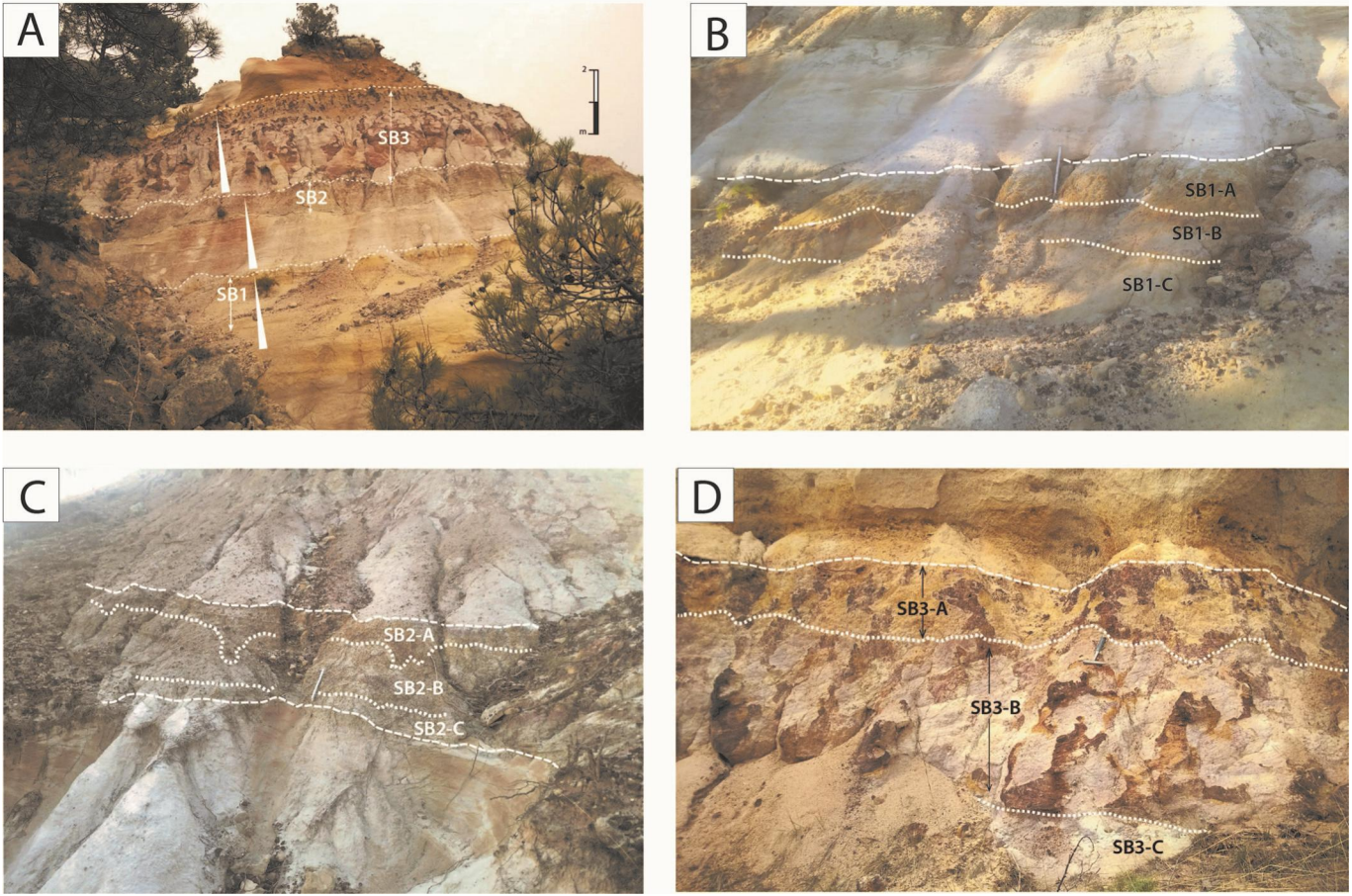
A
SB3
SB2
SB1
2
m
B
SB1-A
SB1-B
SB1-C
C
SB2-A
SB2-B
SB2-C
D
SB3-A
SB3-B
SB3-C

Figure 5

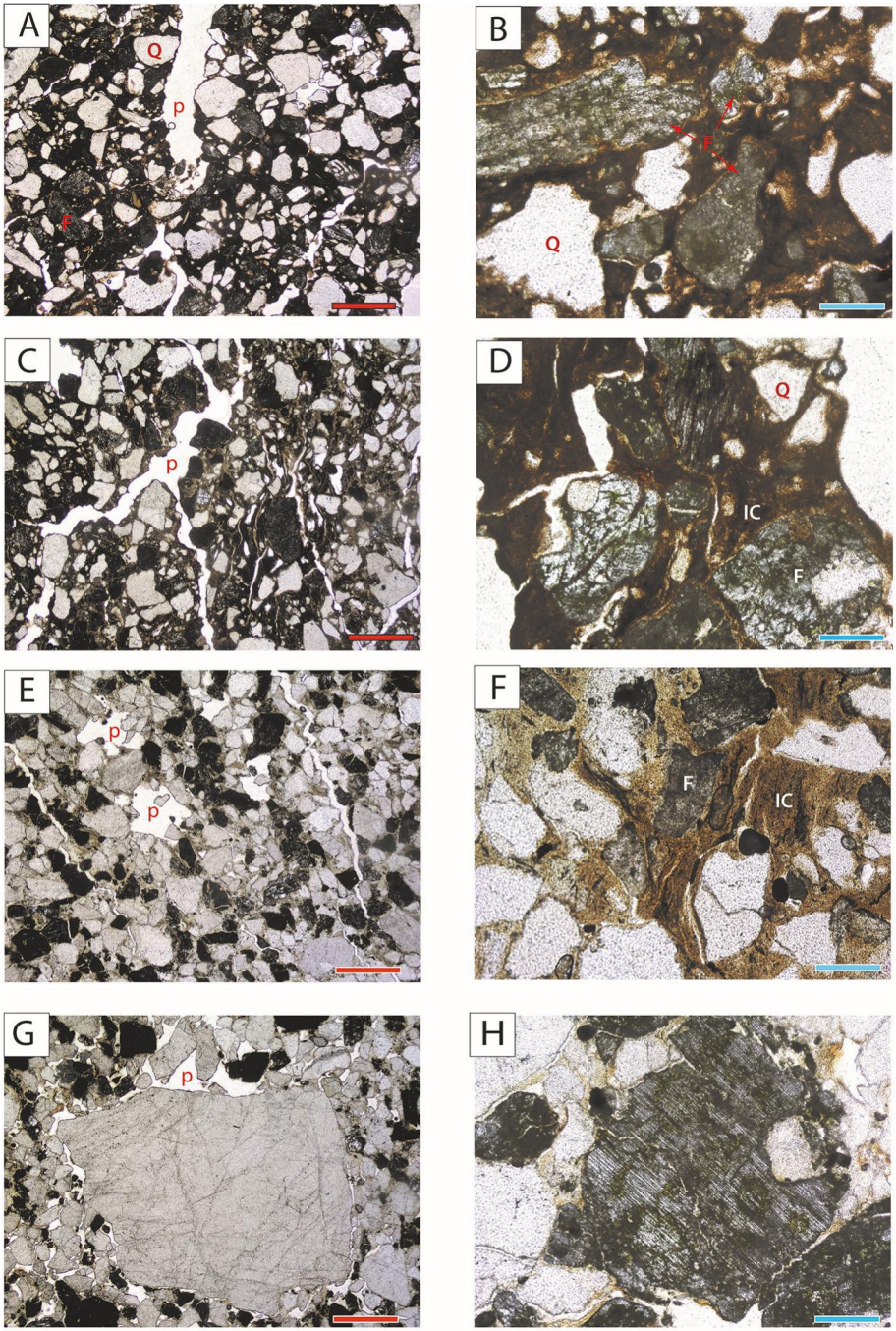

Figure 6

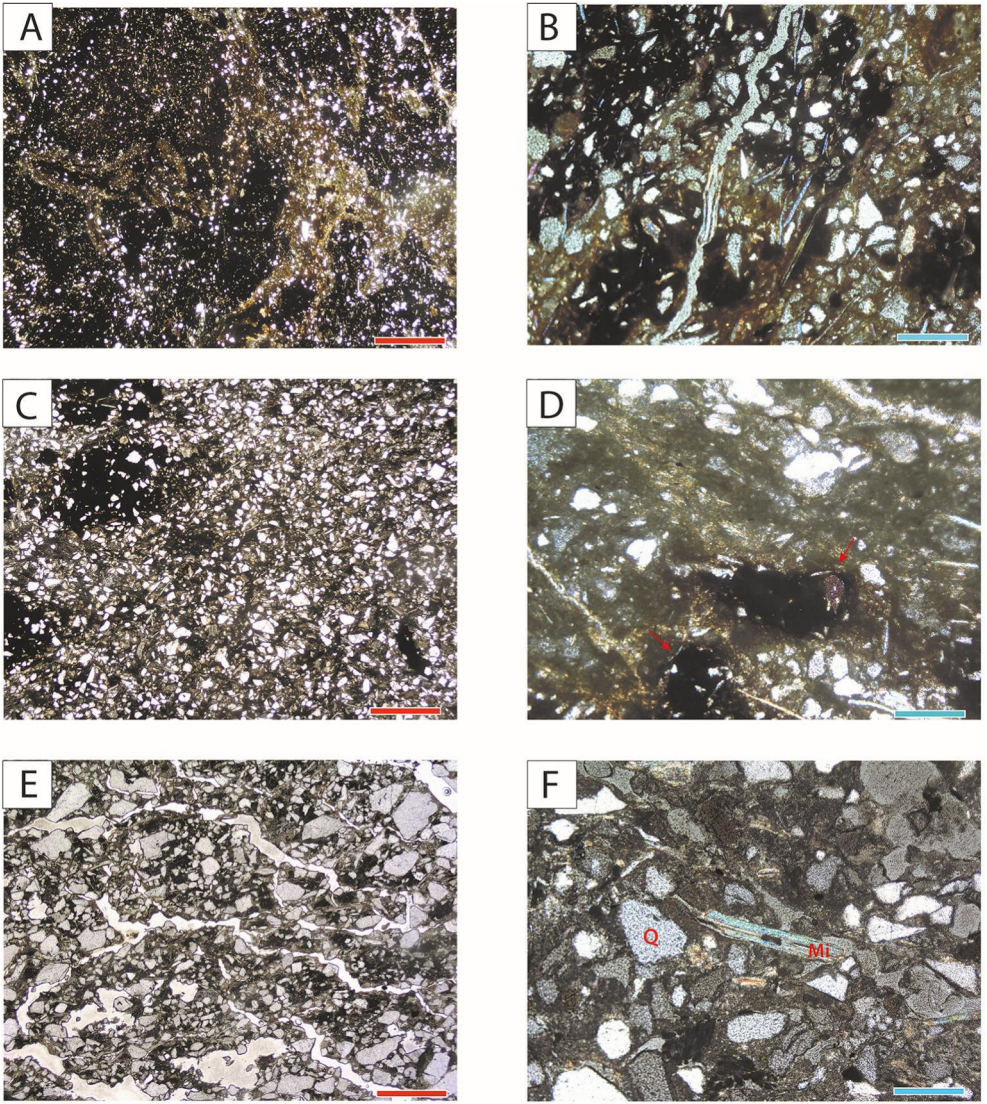

Figure 7

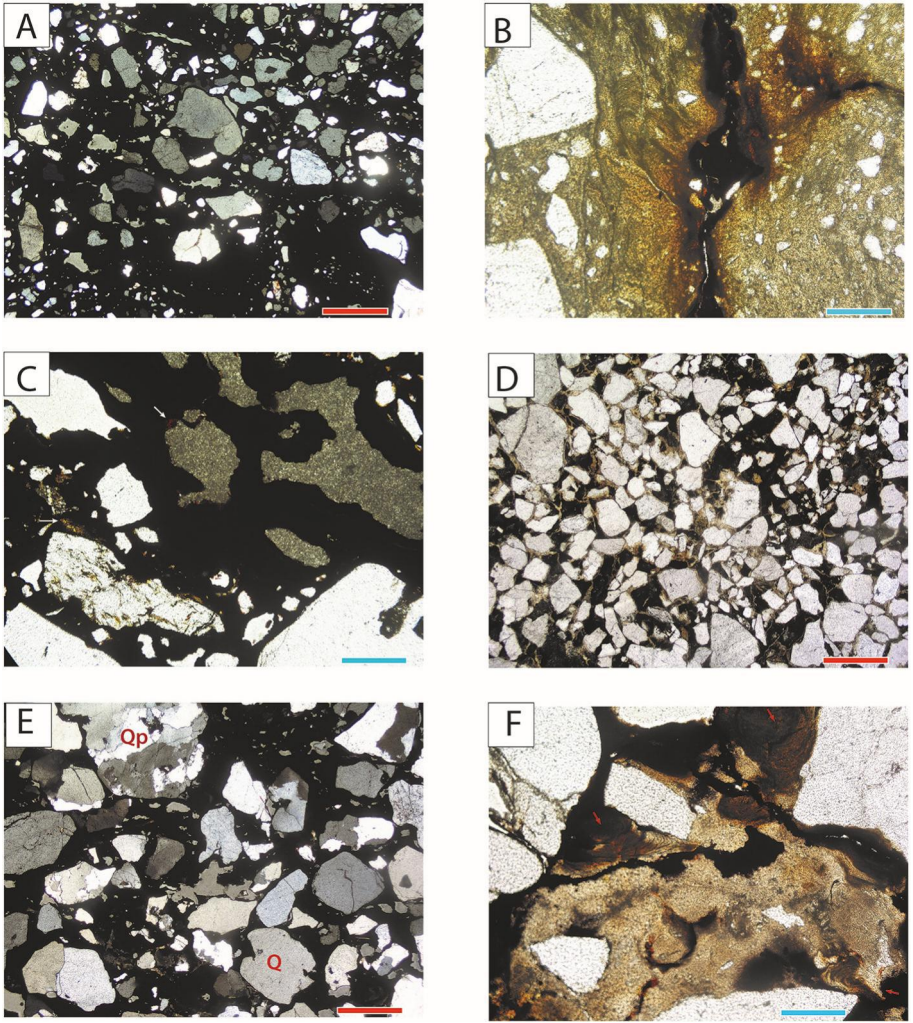

Figure 8

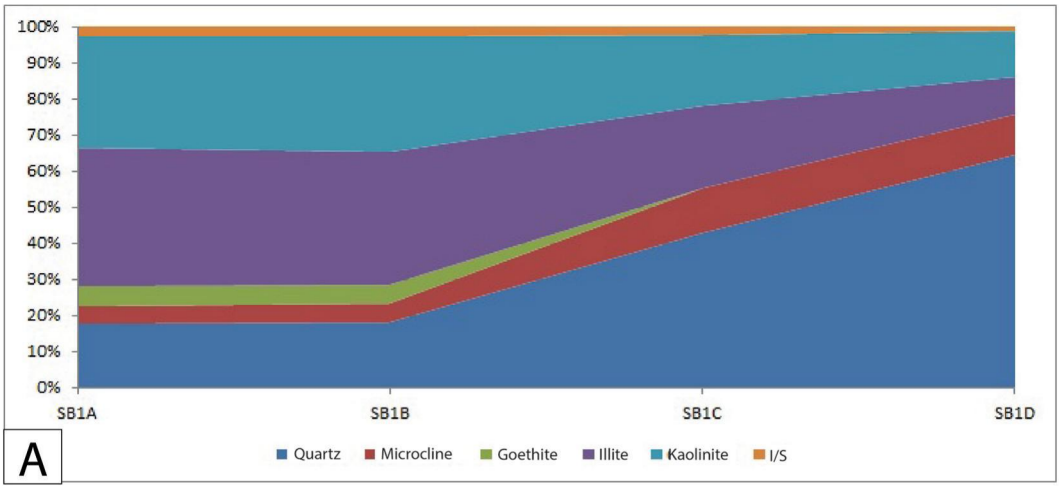
100%
90%
80%
70%
60%
50%
40%
30%
20%
10%
0%
SB1A
SB1B
SB1C
SB1D
A
Quartz
Microcline
Goethite
Illite
Kaolinite
I/S

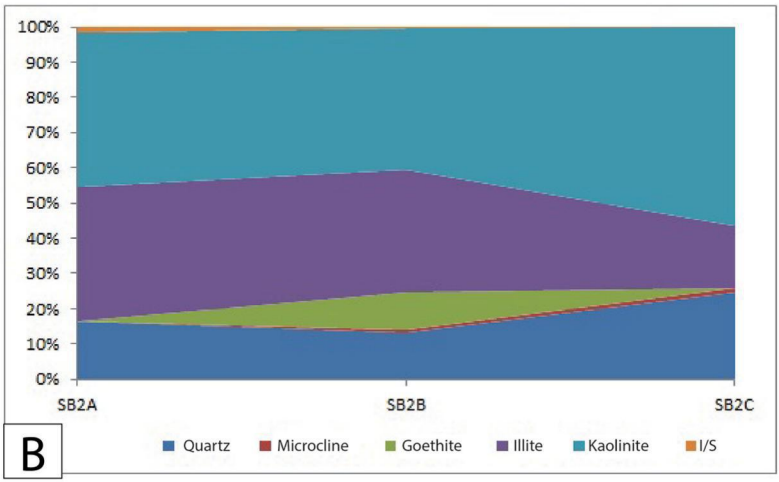
100%
90%
80%
70%
60%
50%
40%
30%
20%
10%
0%
SB2A
SB2B
SB2C
B
Quartz
Microcline
Goethite
Illite
Kaolinite
I/S

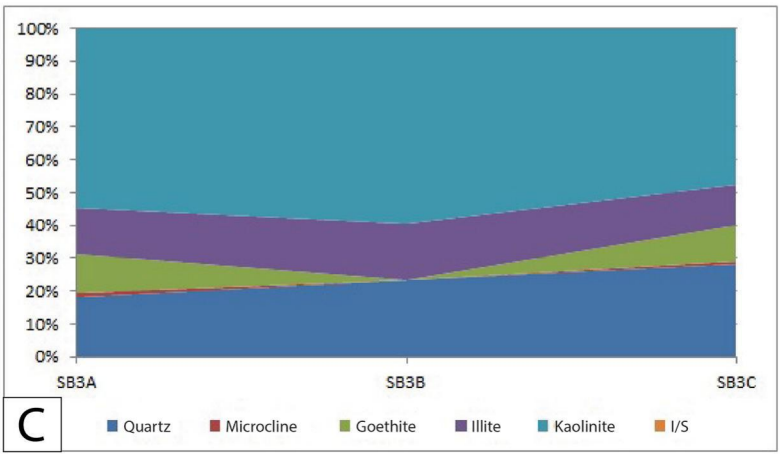
100%
90%
80%
70%
60%
50%
40%
30%
20%
10%
0%
SB3A
SB3B
SB3C
C
Quartz
Microcline
Goethite
Illite
Kaolinite
I/S

Figure 9

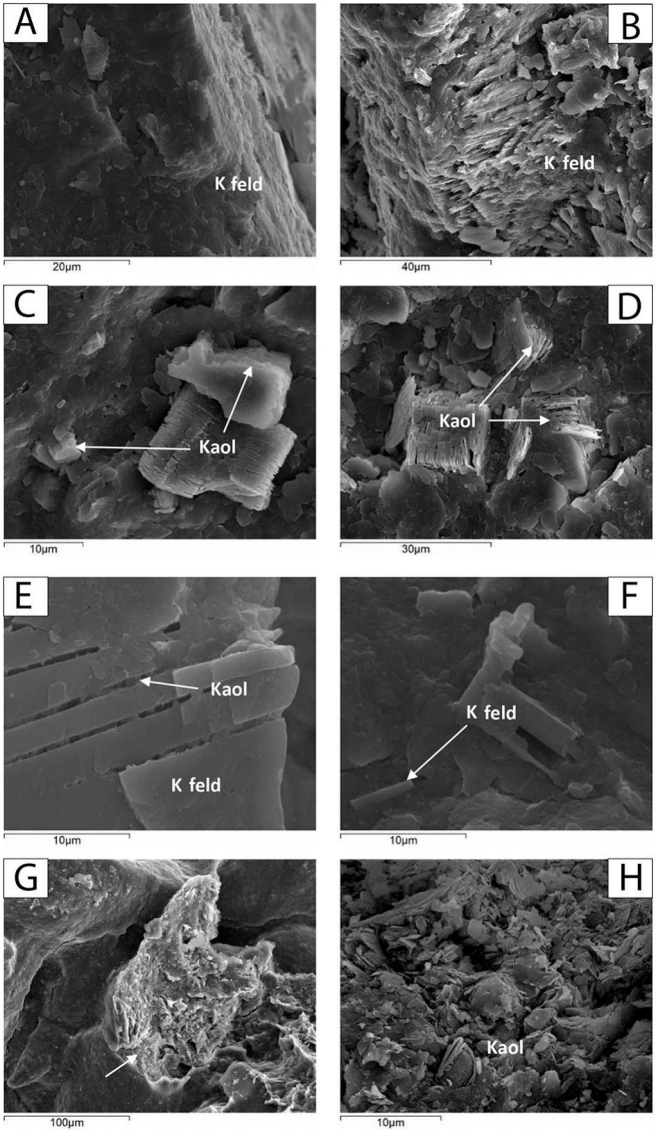
A
K feld
20µm
B
K feld
40µm
C
Kaol
10µm
D
Kaol
30µm
E
Kaol
K feld
10µm
F
K feld
10µm
G
100µm
H
Kaol
10µm

Figure 10

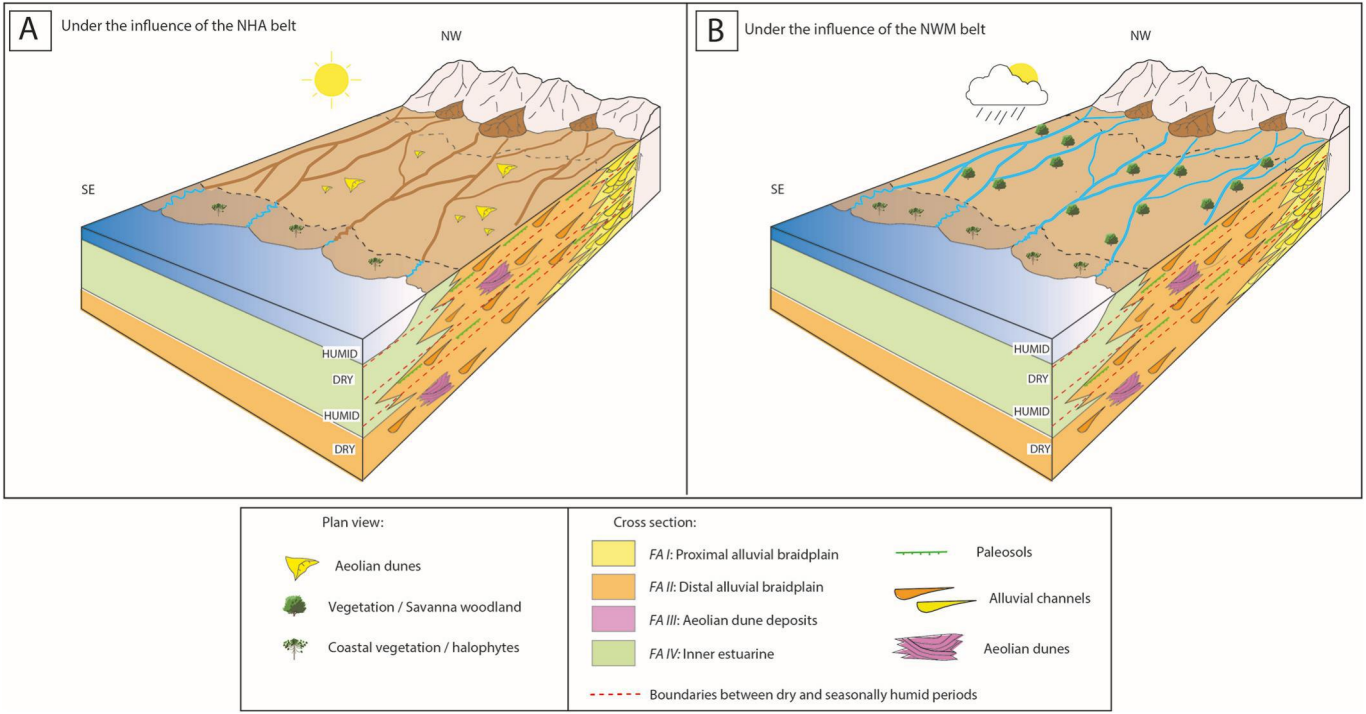
A
Under the influence of the NHA belt
NW
SE
HUMID
DRY
HUMID
DRY
B
Under the influence of the NWM belt
NW
SE
HUMID
DRY
HUMID
DRY
Plan view:
Aeolian dunes
Vegetation / Savanna woodland
Coastal vegetation / halophytes
Cross section:
FA I: Proximal alluvial braidplain
FA II: Distal alluvial braidplain
FA III: Aeolian dune deposits
FA IV: Inner estuarine
Paleosols
Alluvial channels
Aeolian dunes
Boundaries between dry and seasonally humid periods

Figure 11

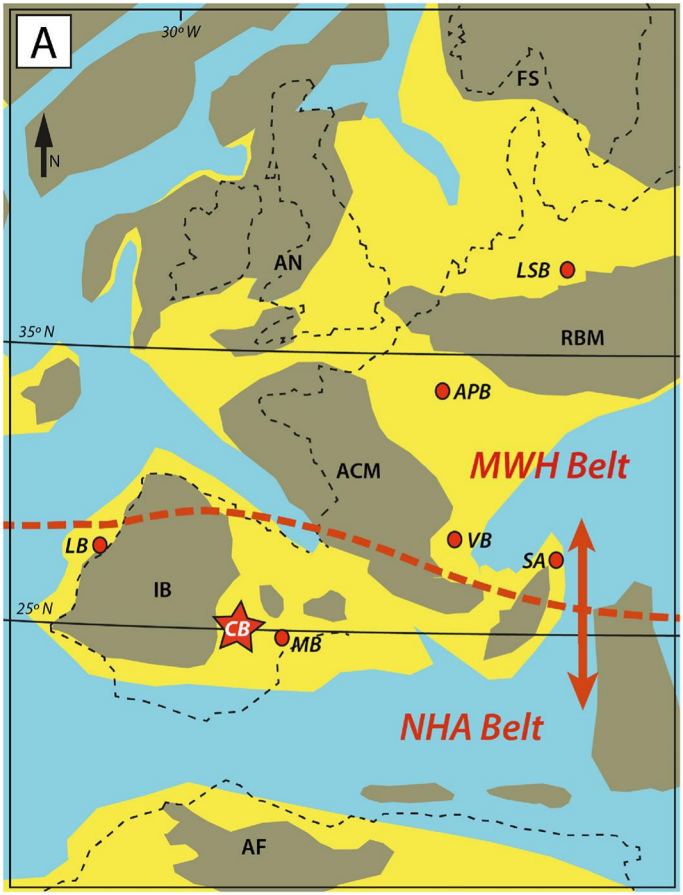

B

	Mineralogical & Geochemical	Sedimentological	Palaeobotanical	References
Lusitanian Basin	Change towards more arid conditions during the mid- to late Albian based on clay mineralogy data.	-	Dominance of xerophytic palynofloras during the mid- to late Albian.	Heimhofer et al. (2012)
Ardennes-Paris Basin	Identification of a semi-arid phase during the mid- to late Albian based on clay mineralogy data.	-	-	Corentin et al. (2020)
Vocontian Basin	Identification of a semi-arid phase during the mid- to late Albian based on clay mineralogy data.	-	-	Corentin et al. (2020)
Lower Saxony Basin	-	Under the influence of the warm humid mid-latitude climate belt during the late Albian.	-	Fenner et al. (2001) and references therein.
"Southern Alps region"	-	-	Presence of N. Gondwanan floral elements in the S. Laurasian floral province.	Hochuli (1981) and refernces therein.
Maestrazgo Basin	-	Development of an erg system (aeolian sand dunes) during the late Albian.	Great plant biodiversity in an arid setting. Dominance of xeric plant communities during the late Albian.	Rodríguez-López et al. (2008, 2009, 2012) Barrón et al. (2023)
Cuenca Basin	* Development of paleosols indicating a seasonally humid tropical climate that alternated in time with the prevalent drier climate conditions.	* Ephemeral alluvial braidplain system with local occurrence of aeolian dunes.	Dominance of xero-phytic palynological assemblages during the mid-Albian to earliest Cenomanian.	Bueno-Cebollada and Meléndez (2018) Bueno-Cebollada et al. (2021) Bueno-Cebollada (2022) **This paper*

Figure 12